The Improvement of Resolution on the Ultrasonic Inspection Method

AUTHOR(S):

ASHIDA, Yuzuru

CITATION:

ASHIDA, Yuzuru. The Improvement of Resolution on the Ultrasonic Inspection Method. Memoirs of the Faculty of Engineering, Kyoto University 1988, 50(2): 37-81

ISSUE DATE:

1988-06-28

URL:

http://hdl.handle.net/2433/281370

The Improvement of Resolution on the Ultrasonic Inspection Method

by

Yuzuru ASHIDA

(Received December 24, 1987)

Abstract

Several data processing techniques used in petroleum exploration are applied to ultrasonic data to enhance resolution and signal to noise ratio.

First, in the case of a medium of low absorption characteristics, the effectiveness of a wavelet processing, a deconvolution filter and a CDP stack is demonstrated.

Second, in the case of a medium of high absorption characteristics, an attenuation coefficient is estimated using the spectrum ratio method. Waveforms at an arbitrary depth can be synthesized by the estimated attenuation coefficient and the reflected wave at the reference depth. Wavelet processing, which utilizes the synthesized wavelets at each depth as the new basic wavelet including the absorption characteristics, greatly improves resolution.

Finally, the wavelet processing, the migration processing and the synthetic acoustic impedance log are applied to the data from a phantom model which exhibits ultrasound responses similar to those in a human liver. The fluid-filled objects, 10 mm in diameter, are not only resolved, but the polarity and phase information in the reflected waves is also preserved through these processings.

Consequently, it is concluded that pin-holes in metals or small size cysts or tumors in a human body are detectable by the enhancement of resolution of ultrasonic diagnosis.

1. Introduction

Ultrasonic inspection methods are frequently used in the field of medical diagnosis and non-destructive metal inspection. Especially, the pulse-echo method in ultrasonic inspection methods observes the reflected waves from the boundaries between the tissues in a human body. Hence, the pulse-echo method belongs to the same category as the reflection method for subsurface exploration. Therefore, the advanced techniques of the reflection method for petroleum exploration are applicable.

* Department of Mineral Science and Technology

The vertical resolution of direction to depth is very important in ultrasonic inspection methods. Although this resolution can be improved by generating an impulse shaped waveform, the generation of a single impulse has not yet been realized.

The dynamic range of ultrasonic diagnostic data extends over 100 ~ 120 dB. The current diagnostic equipment rectifies the detected reflection waves and displays the logarithm of its envelope on a Braun tube[1]. Consequently, this procedure not only sharply degrades resolution, but also the important information of polarity and phase is lost. It is epochmaking to improve a sharply resolution and to preserve the information of polarity and phase, using the current ultrasonic diagnostic equipment.

This paper describes the enhancement of resolution of ultrasonic inspection methods by applying several data processing techniques used in petroleum exploration to three kinds of media: a medium of low absorption characteristics, a medium of high absorption characteristics and a multipurpose tissue/cyst phantom.

2. Equipment Used

Figure 1 shows the experimental set-up. The specifications of the ultrasonic diagnostic equipment and the analog to the digital converter are shown in Table 1. The reflected waves are recorded on a floppy disk in the mini-computer after passing through an alias filter and the A/D converter.

The probe contains sixty-four elements which can transmit ultrasonic waves

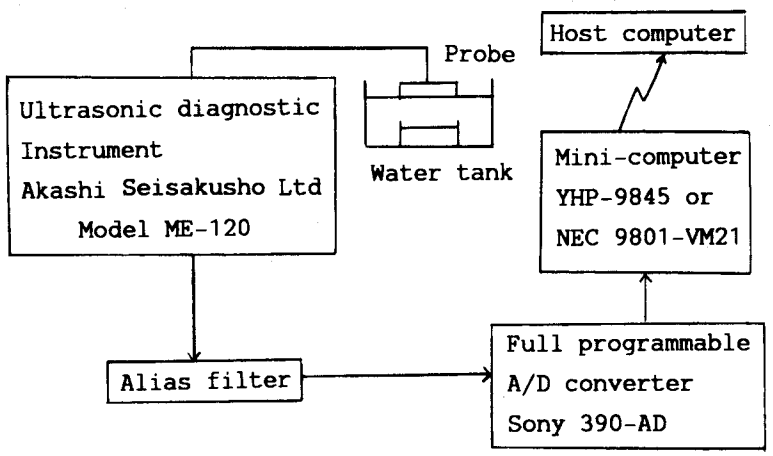

Fig. 1 Block diagram of experimental instruments

Table 1 Ultrasonic diagnostic equipment and Analog to Digital converter specification

Ultrasonic diagnostic equipment	
• Scan method	Electronic linear scan
• Frequency	3.5MHz
• Scan width	90㎜
• Penetration	160㎜
• Amplifier	Logarithmic
A/D Converter	
• Resolution	10 Bits
• Maximum sample rate	60MHz for 1 Channel
	30MHz for 2 Channels
• Sensitivity	±100Mv~50V

and receive signals that have 1.6㎜ intervals. The A/D converter can simultaneously handle up to 6 channels. The total system is controlled by an NEC 9801 XL or a YHP-9845 mini-computer. The data recorded on the floppy disk are transmitted to the main computer through an exclusive use circuit and submitted to data processing.

3. Experiment with a Medium of Low Absorption Characteristics

3.1. Effectiveness of the wavelet processing

An acrylic plate, 20㎜ in thickness with a hole 5㎜ in diameter and attached to an aluminum plate 10㎜ in thickness, was prepared for the experiment. The top of the model, shown in Figure 2, was placed in water at a depth of 41.5㎜. The data for the CDP (Common Depth Point) stack[2] were acquired in order to indicate the effectiveness of a wavelet processing, using survey parameters shown in Table 2. The thirty-second element in a probe was used as a transmitter, and four elements from the twenty-ninth to the thirty-second were also used as receivers. While the transmitter and the receivers were moving over the model with a half of the element interval or 0.8㎜, the thirty-four records were acquired. The shot point numbers and the CDP numbers are shown at the top of Figure 2.

Figure 3 shows the zero offset trace in the first CDP to which several data processing methods are applied. A-1 and B-1 in Figure 3 are the original records without any data processing. Three reflected waves appear, which show a reflection from the top surface of the acrylic plate approximately 57 to 60 μs in time, one from the boundary between the acrylic plate and the aluminum plate

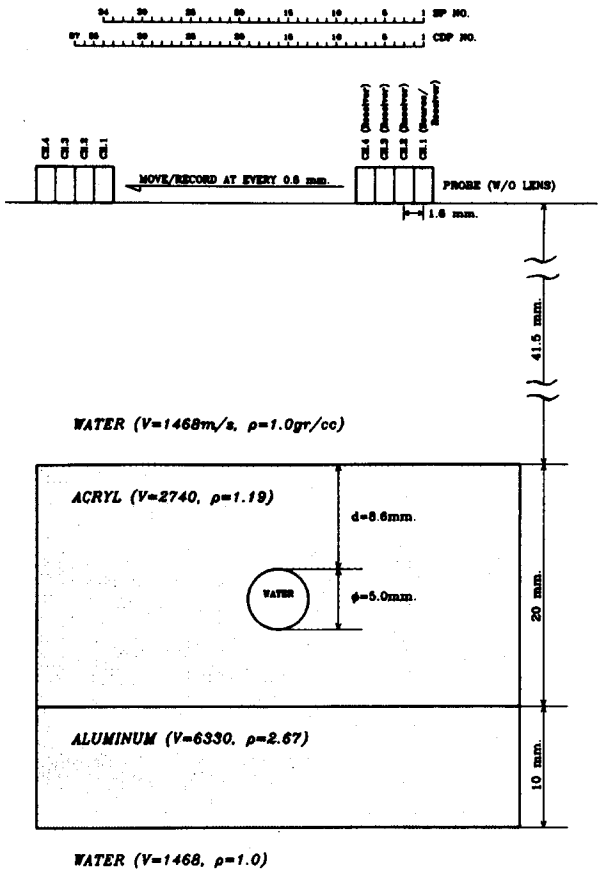

Fig. 2 Schematic diagram of data acquisition geometry

Table 2 Survey parameters for CDP stack

NO. of channels	4
Channel intervals	1.6mm
Shot point intervals	0.8mm
CDP multiplicity	400%
Acoustic lens	No
Electronic focus	No

between 71.5 to 74 μs and a reflection from the bottom surface of the aluminum plate close 75 μs. A-2 shows the result when a whitening deconvolution filter[3] is applied to A-1. A-3 and A-4 are applied in turn a band pass filter and amplitude correction to A-2. The A-2 output from the whitening deconvolution filter is not necessarily the impulse of the desired wavelet. This means that

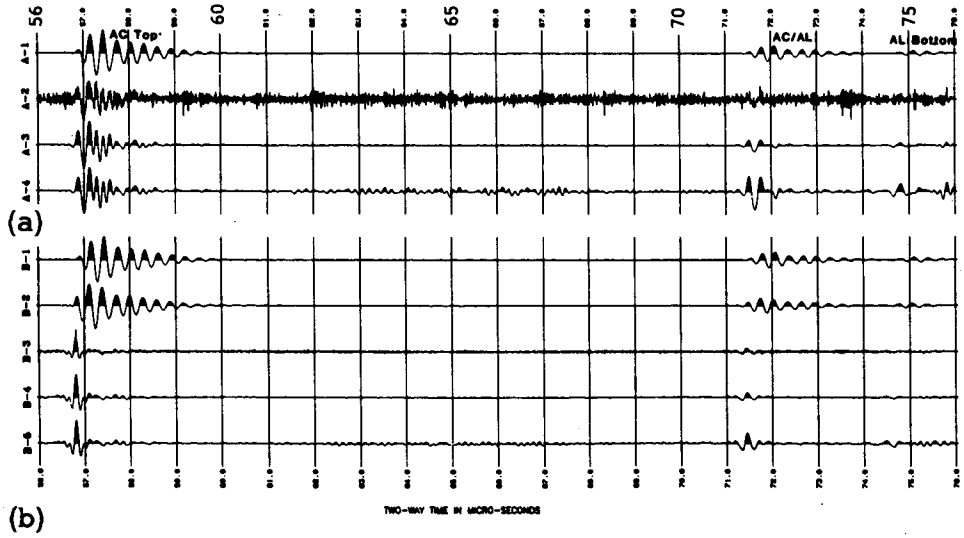

Fig. 3 Comparison between whitening deconvolution filter and wavelet processing
(a) record after applying whitening deconvolution filter
(b) record after applying wavelet processing

the waveforms in A-1 do not satisfy the minimum phase characteristics required for the deconvolution filter.

On the other hand, B-2 shows the result when a wavelet processing[4] is applied to B-1. There, a basic wavelet is defined as the impulse response of the total characteristics including the characteristics of the transmitter, receiver and diagnostic instrument. The basic wavelet is extracted from the isolated reflected wave at the top surface of the acrylic plate. The desired wavelet is the wavelet whose ampltude spectrum is the same as a basic wavelet, and whose phase spectrum is minimum phase. B-3, B-4 and B-5 are applied in turn a whitening deconvolution filter, a band pass filter and an amplitude correction to B-2. Comparison of A-4 with B-5 shows that each reflection in B-5 is very close to the impulse. This means that the resolution improved sharply. Since the time that the impulse stands after wavelet processing is equal to the arrival time of the wavelet, the accurate depth to the reflection boundary can be computed from the correct arrival time.

Consider the wavelet processing from the spectrum point of view. Figure 4 (a) shows the power spectrum ranging from 0 to 50 MHz for the portion 56 to 61 μs of the original record B-1 in Figure 3. This shows that the frequency

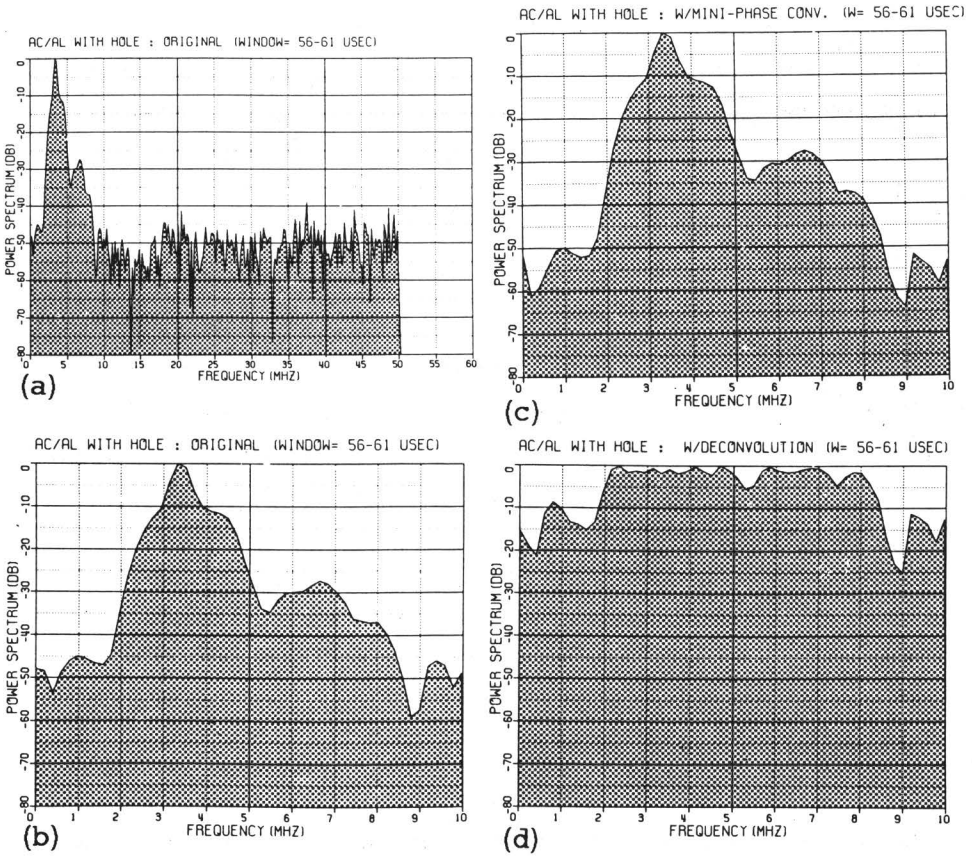

Fig. 4 Power Spectra
(a) original reflected wave
(b) enlargement of portion (a)
(c) after applying minimum phase conversion
(d) after applying whitening deconvolution filter

range of the ultrasonic diagnostic system is narrowly limited to approximately 3.3 MHz, and the frequency components out of 2 to 8 MHz range fall into a noise level below − 40 dB from the signal. Figure 4 (b) is the enlargement of the 0 to 10 MHz portion of Figure 4 (a). Figure 4 (c) shows the power spectrum of B-2 in Figure 3 after the wavelet processing by the minimum phase conversion. Since the power spectrum in Figure 4 (c) is almost the same as the one in Figure 4 (b), it is concluded that the wavelet processing by the minimum phase conversion corrects only the phase lag. Figure 4 (d) shows that the power spectrum of B-3 in Figure 3 has been flattened by applying a

whitening deconvolution filter. This demonstrates that the reflected wave of B-3 in Figure 3 has been converted to an impulse.

The extraction of the basic wavelet is very important in wavelet processing. If the basic wavelet changes at each shot, one for each shot must be extracted, which makes the wavelet processing unpractical. Therefore, referring to Figure 5, consider the stability of the basic wavelet in the present system. Figure 5 (a) shows a single waveform. Figure 5 (b) to (d) shows the vertically stacked waveforms of 1,000, 2,000, 3,000%, respectively. The cross correlation coefficients are computed between the waveform in Fig 5 (a) and one from (b), (c) or (d) in order to confirm the stability of the waveform at each shot. The results are shown in Table 3. Cross correlation coefficients higher than 0.95 show that the transmitter generates almost the same waveform at each shot. Therefore, once a basic wavelet has been extracted, it can be used throughout the wavelet processing, assuming that the same transmitter is used. In the present experiment, the vertically stacked waveform of 1,000% was adopted as the basic wavelet.

As above mentioned, sharp improvement in resolution can be expected since the record section where an impulse is transmitted into a medium, can be acquired by the wavelet processing.

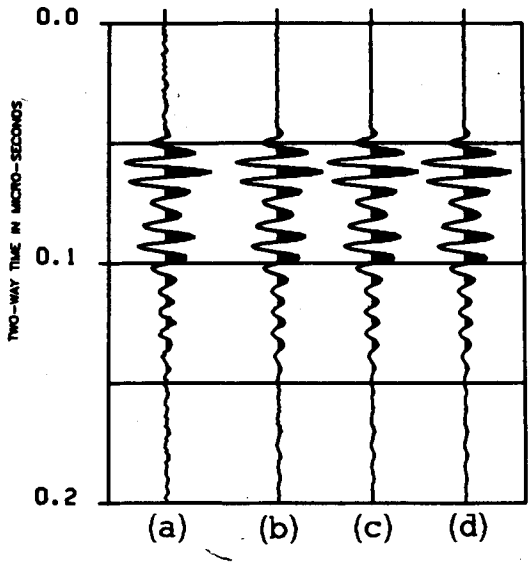

Fig. 5 Waves generated from ultrasonic transmitter
(a) single wave
(b) vertically stacked wave of 1,000%
(c) vertically stacked wave of 2,000%
(d) vertically stacked wave of 3,000%

Table 3 Cross correlation coefficients at time lag 0 between waves (a) and (b), (c), (d) in Fig. 5

	(b)	(c)	(d)
(a)	0.9668	0.9904	0.9913

3. 2. **Experiment for a model with a hole**

Figure 6 shows records taken over the hole of the model illustrated in Figure 2. Here, the records from the 8 th to the 22 nd shot points are selected.

Figure 7 (a) shows the near trace section selected from the CDP stack data. Figure 7 (b) to (e) shows the some section after a wavelet processing by a minimum phase conversion, where a whitening deconvolution filter, a band pass filter and an amplitude correction are applied in turn to the near trace section. Comparison of Figure 7 (a) with (e) shows that record quality is improved when the sidelobe is removed by the wavelet processing.

On the other hand, Figure 8 shows the final record section in which a CDP stack including a wavelet processing is applied. The data processing sequence is a CDP gather, a wavelet processing by the minimum phase conversion, a whitening deconvolution filter, a normal move out correction, a CDP stack, a band pass filter and finally an amplitude correction. The velocities for the normal move out correction are determined from the velocity analysis[5], using the constant velocity gather method which is performed every four CDPs from CDP number 4 to 34. The velocity analysis at CDP number 24 is shown in Figure 9, and the root mean square velocities with travel times are shown in Table 4. There appears no difference between the 400% coverage CDP stack section in Figure 8 and the single coverage section in Figure 7 (e). The reason for this may be that the acquired data contain a little noise whose frequency band differed from the signal, and was therefore removed by a band pass filter. However, the merit for acquiring the CDP stack data is that velocity information can be obtained.

Figure 10 represents the display of the near trace section of Fig 7 (a), using a current ultrasonic diagnostic instrument. That is, an envelope logarithm, computed from the rectified near trace by a complex seismic trace analysis[6], is displayed using a display mode of wiggle trace superimposed on a variable area. The Figure 8 record section, where a wavelet processing and a CDP stack are applied, shows a much higher resolution than that of Figure 10.

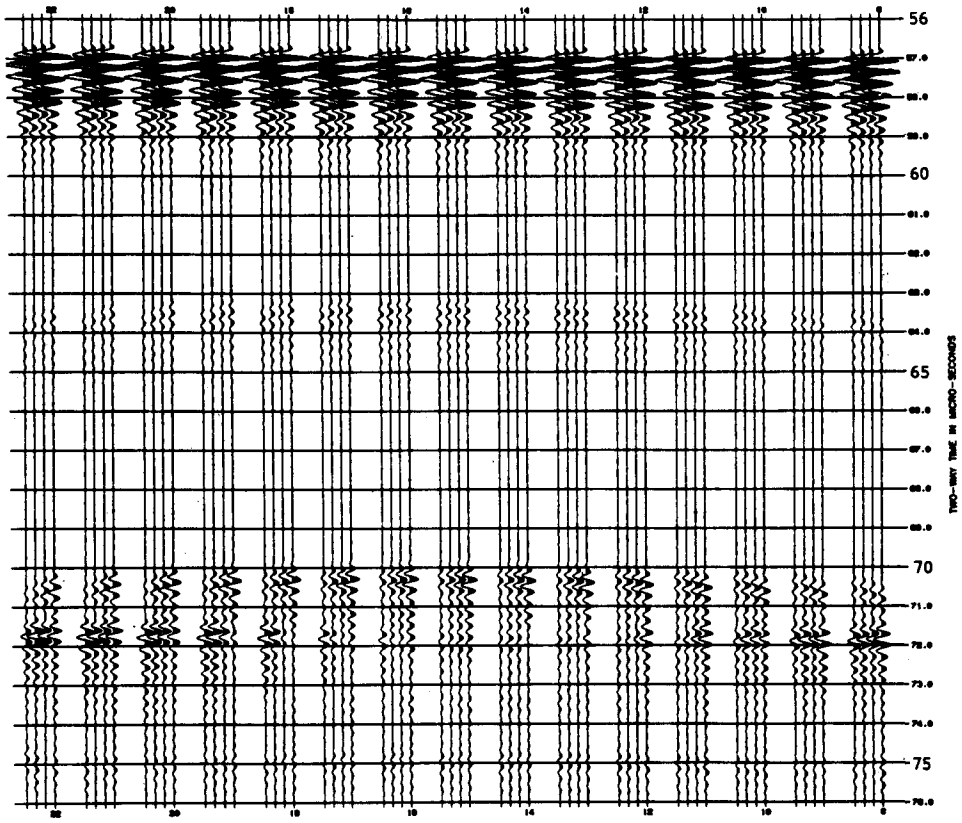

Fig. 6 Records from the 8 th to the 22 nd shot points over a hole in the model

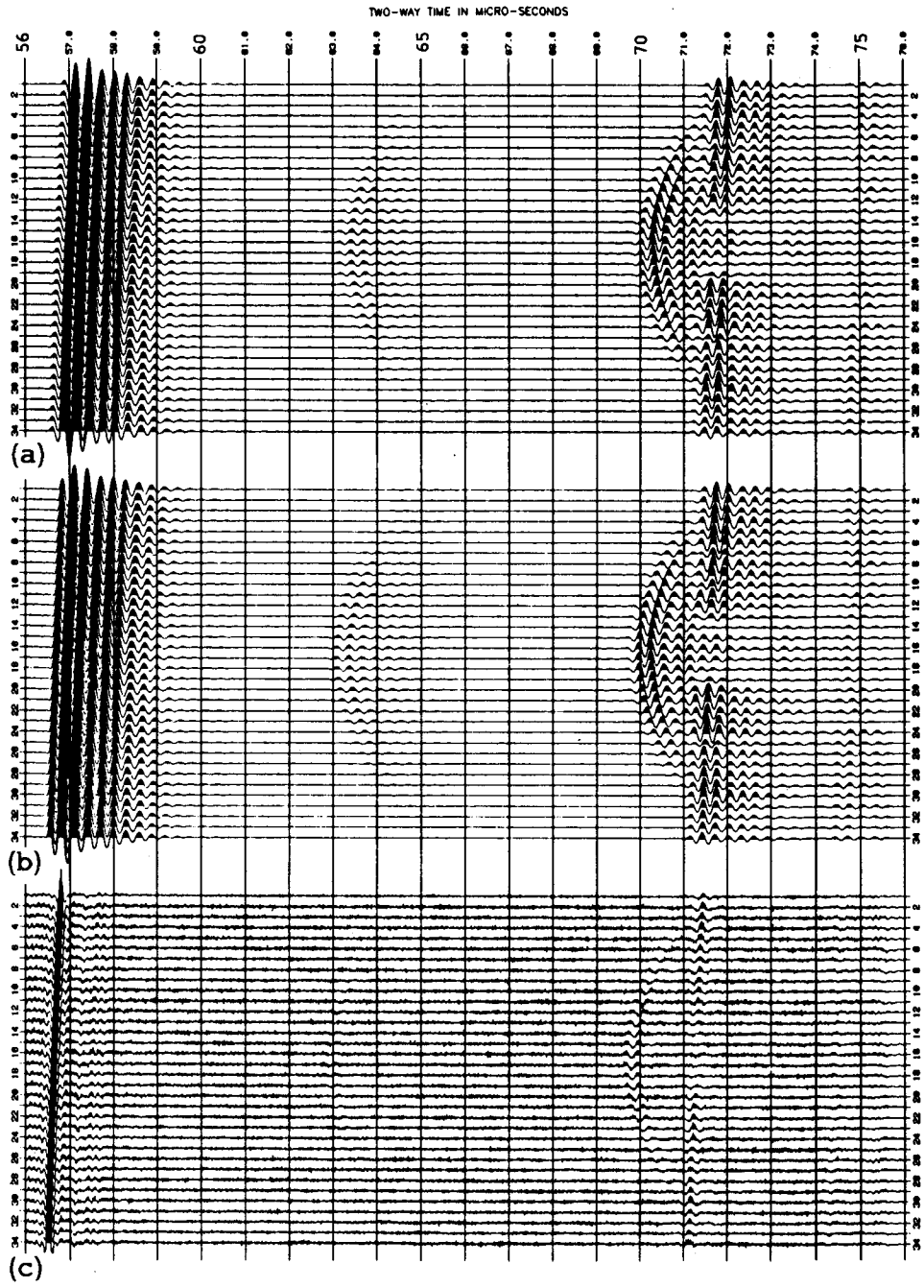
TWO-WAY TIME IN MICRO-SECONDS
56
57.0
58.0
59.0
60
61.0
62.0
63.0
64.0
65
66.0
67.0
68.0
69.0
70
71.0
72.0
73.0
74.0
75
76.0
(a)
(b)
(c)

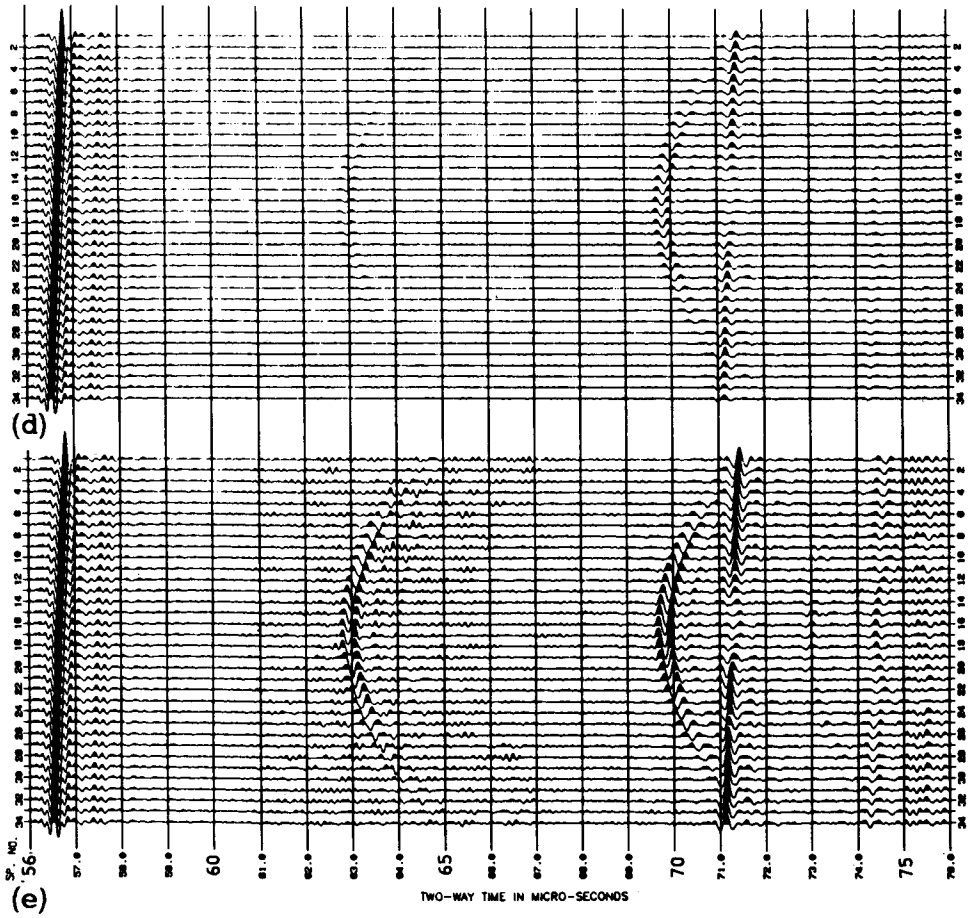

Fig. 7 Display of near trace section according to the processing sequence for wavelet processing

(a) near trace section rearranged from shot base record section in Fig. 6

(b) after applying wavelet processing by minimum phase conversion to (a)

(c) after applying whitening deconvolution filter to (b)

(d) after applying band pass filter to (c)

(e) after applying amplitude correction to (d)

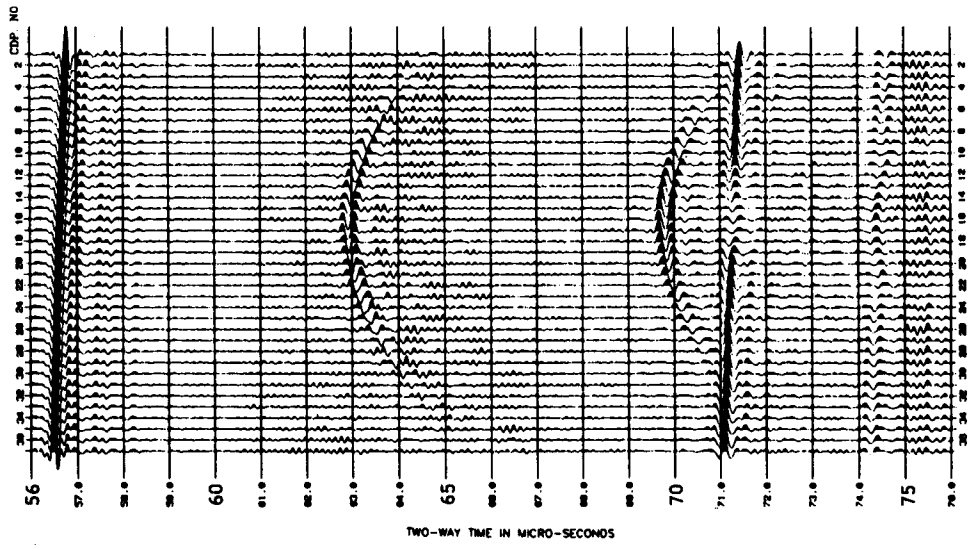

Fig. 8 Display of record section after wavelet processing and CDP stack have been applied

Table 4 Stacking velocities determined from velocity analysis

Time(ns)	Rms Velocity(m/s)
56,600	1,550
63,300	1,500
70,000	2,000
71,400	2,800
74,400	2,200

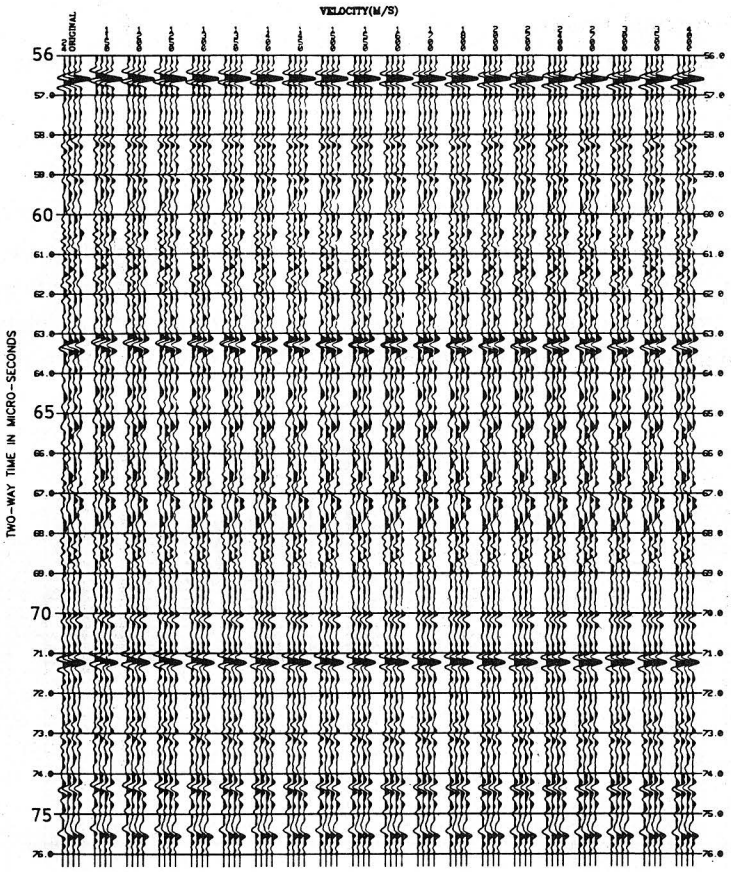

Fig. 9 Velocity analysis display

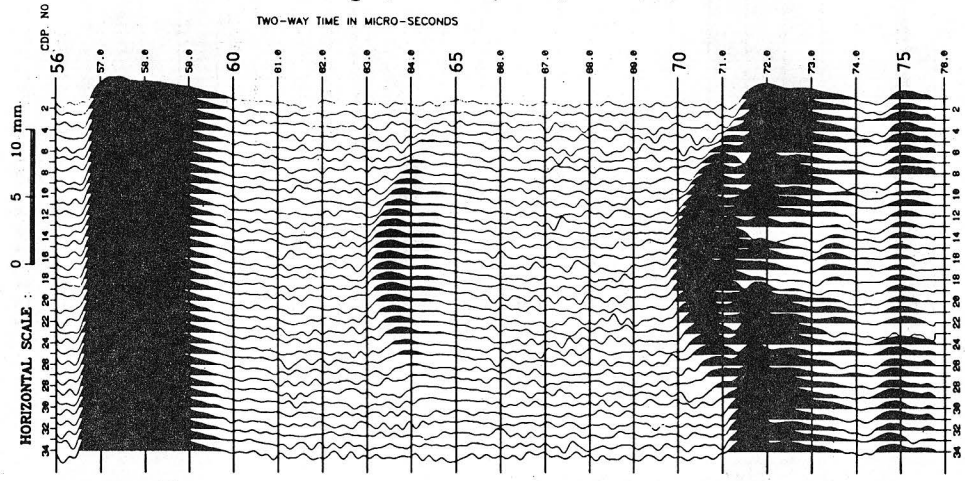

Fig. 10 Near trace section with display method in current ultrasonic diagnostic instrument

3. 3. **Experimental results**

Here, each Figure 8 reflection event will be related to the boundary of the model shown in Figure 2.

Figure 11(a) is the same as Figure 8, except that reflection events are now labeled by A–A′, B, C, D–D′, d, E–E′. The positive polarized reflected wave, A–A′, is from the top surface of the acrylic plate. The retrogression of the wave from A to A′ shows that the model was not set up completely parallel to the surface of the water. The negative polarized, semi-circular reflected wave indicated by B is the reflection from the top of the water-filled hole in the acrylic plate. Though the arc-shaped reflected wave indicated by C looks upwards like a convex shape

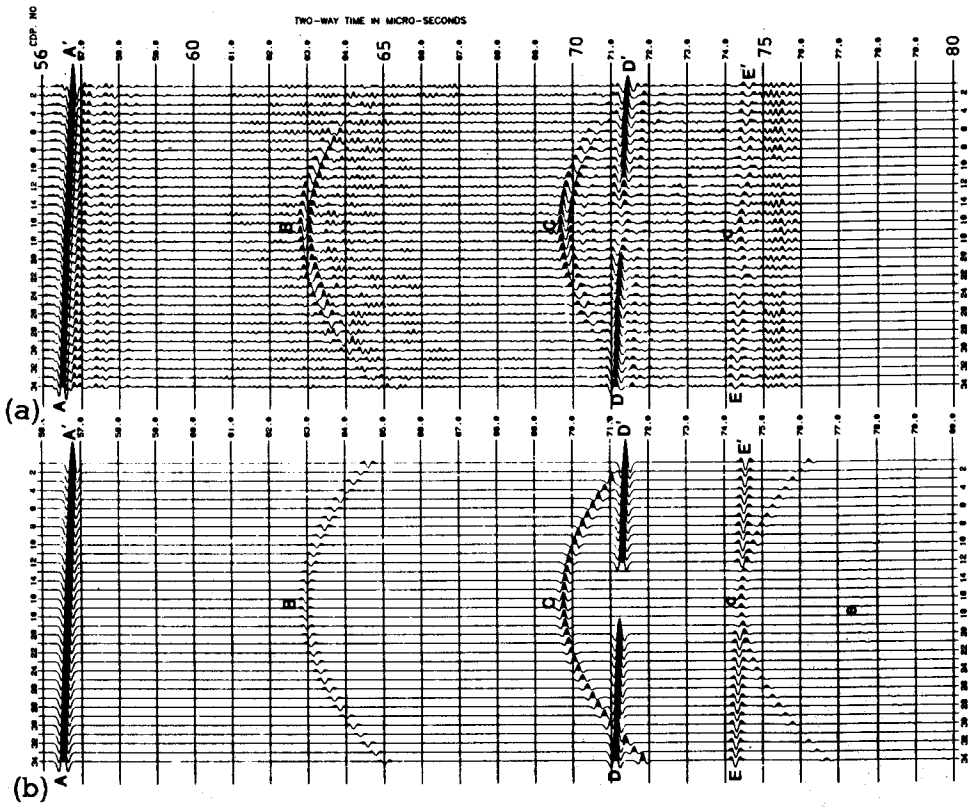

Fig. 11 Comparison between observed CDP stack record and model calculation result

(a) observed CDP stack record

(b) result calculated by ray tracing method

in the record section, it is actually the reflection from the bottom of the hole. The polarity of this reflection is examined later in the next paragraph 3.4.. Judging from the record section before the amplitude correction in Figure 7 (d), the reflection from the top of the hole has a larger amplitude than the one from the bottem of the hole. It may be that the former acts as a convex mirror and the latter as a concave mirror. The positive polarized reflected wave indicated by D–D′ is the boundary reflection between the acrylic and the aluminum plate. The negative polarized reflected wave indicated E–E′ indicates the boundary between the aluminum plate and the water. Analysis of Figure 11(a) reveals the following unusal phenomena:

(i) The central portion of the reflected wave indicated by D–D′ disappears.

(ii) The positive polarized convex shape wave indicated by d appears in the central part of the reflection of the bottom of the the aluminum plate.

In order to examine these phenomena, a record section synthesized by a ray trace modeling method was compared with the observed record section.

3. 4. **Model calculation by ray tracing method**

The ray tracing procedure[7][8] is as follows:

(i) Calculate the ray path from a shot point to a receiving point using Snell's law for a given structure feature and velocity distribution.

(ii) Divide the length of the ray path in each layer by its velocity and sum up the quotients for each layer so as to get the travel time for each receiving point.

(iii) Set the impulses whose amplitudes are equal to the reflection coefficients of each boundary at the position of the calculated travel times for each receiving point.

(iv) Convolve a suitable wavelet, such as a Ricker wavelet, with the above reflection time series to get a synthetic record section.

Figure 12 shows the neighboring part of a model of the calculated ray path. The values of density and velocity for water, acrylic and aluminum were assumed to be 1.0, 1.19 and 2.67 g/cm^3 and 1,468, 2,740 and 6,330 m/s, respectively. Figure 11 (b) shows the record section synthesized by a ray tracing method. Here, a Ricker wavelet with a peak frequency of 3.3 MHz was adopted as the wavelet to be convolved with the reflection time series. The travel times and reflected waves of Figure 11(a) and (b) show good correlation, excluding the noise in Figure 11(a). The phenomenon of the small amplitude of the central portion of reflection D–D′ and the wave indicated by d are analysed as follows: The rays bound for the D–D′ boundary directly beneath the hole in the model are delayed

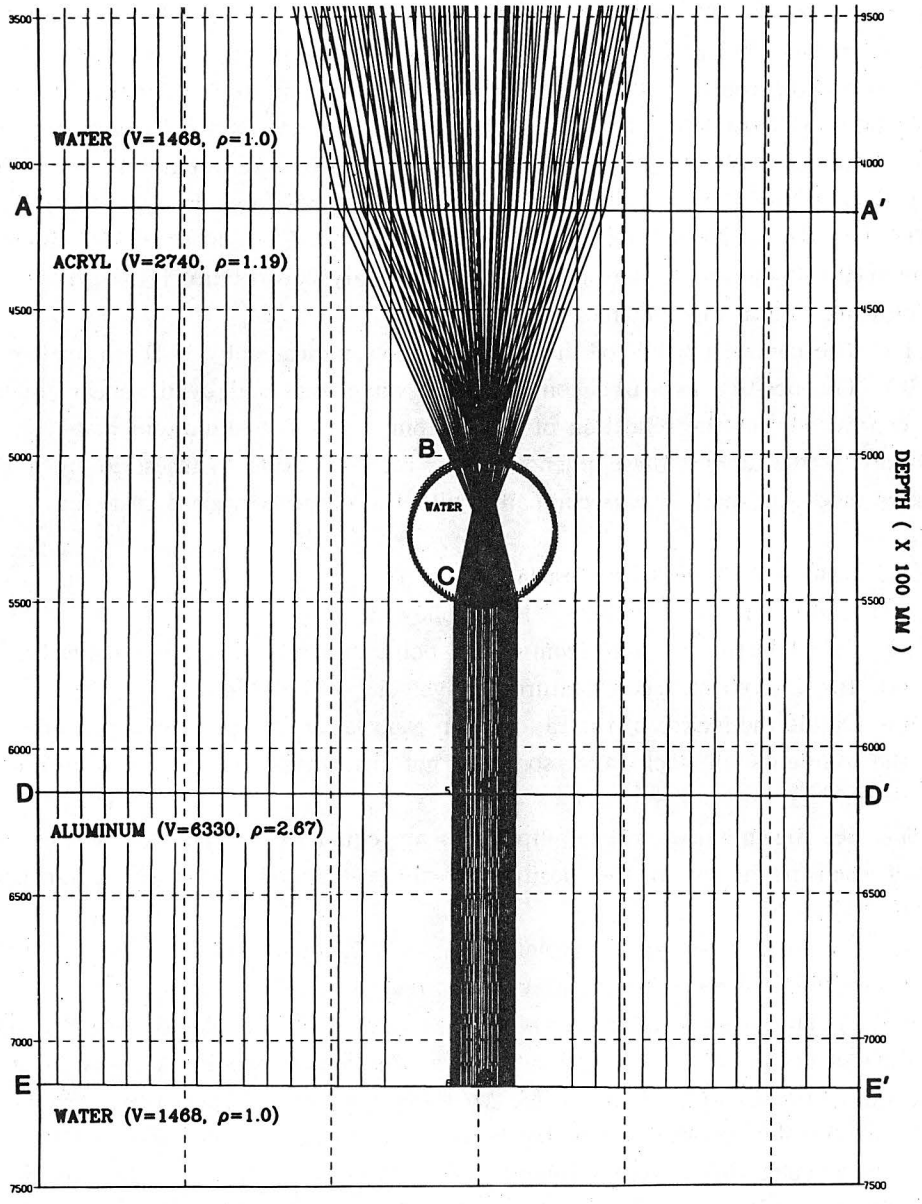

Fig. 12 Normal incidence ray paths deduced from ray tracing method at zero offset

about 3 μs because of the water in the hole. Therefore, the D-D′ reflected waves directly beneath the hole appear at the same time as E-E′, as indicated by d. Also, the reflected wave from the central part of E-E′ is delayed about 3 μs in time. However, it is out of the recording period range in the present experiment.

Consider the phase of reflection C. The phase of the Figure 11(a) waveform obviously differs from the synthetic waveform by a ray tracing method in Figure 11(b). The polarity of reflected wave C in Figure 11(b) was assumed to be positive, because it was reflected from the boundary between the water in the hole and the acrylic plate. Hence, the phase of this reflected wave is the same zero phase as the Ricker wavelet which was convolved to get a synthetic record. On the other hand, the polarity of Figure 11(a) looks negative. Its ray path, as shown in Figure 12, passes through a buried focus in the water-filled hole and should gain in phase[9] by 90°. That is, the convex shape of reflection C corresponds to the reverse branch portion peculiar to a buried focus. Although C reflection should gain in phase by 90° in the observed record, actually the phase progresses by nearly 180° in Figure 11(a). The reason for this phase difference may be that the originally extracted basic wavelet was used without a 90° phase progress in the wavelet processing.

4. Experiment with a Medium of High Absorption Characteristics

4. 1. Ddta acquisition

An acrylic plate, 20 mm thick, was submerged in castor oil having high absorption characteristics. The thirty-second ultrasonic element in a probe is used as a transmitter and a receiver. One record at each depth is observed by setting the acrylic plate at depths of 15.0, 25.5, 36.5, 45.5, 55.0, 65.0 and 75.0 mm from a transmitter. The survey parameters are shown in Table 5. Figure 13 shows the reflected waves from the top surface of the acrylic plate at each depth from the transmitter in castor oil. Here, the amplitude of each trace was

Table 5 Survey parameters using a medium of high absorption characteristics

Transmitter/receiver	No. 32 element
Peak frequency of probe	33MHz
No. of channels	1
Sample rate	60MHz(16.67ns)
Alias filter	No
Acoustic lens	No
Electronic focus	No

normalized with its maximum absolute amplitude. Also, the relative amplitude ratio in dB, which is normalized with a maximum amplitude in a trace at depth of 15.0 mm, is also attached to the upper part of each trace. These values − 22.2 dB at depth 45.5 mm and − 42.9 dB at maximum depth 75.0 mm show that the amplitudes decay to about 1 / 13 and about 1 / 140, respectively. Though the S /N ratio is high up to a depth of 65.0 mm, noise is quite distinguishable at 75.0 mm.

Figure 14 shows the change of waveform with depth. While the first arrivals of waves are aligned, they gradually lengthen with an increase in depth. Power spectra were computed for waves from the top surface of the acrylic plate at each depth. The window length for spectrum calculation was fixed at 4.2 μs from the first arrival for each trace. Figure 15 shows the power spectra normalized with a maximum spectrum value at a frequency of 3.2808 MHz for the depth of 15.0 mm. The peak frequency not only falls from 3.3 to 2.3 MHz, but also the higher frequency components are largely attenuated.

4. 2. **Estimation of absorption characteristics**

The main causes for attenuation[10] of amplitude are:

(i) Spherical divergence of waves
(ii) Absorption by friction or heat loss
(iii) Transmission loss
(iv) Energy loss from scattering effects

Spherical divergence is caused by a wavefront expanding with time and is called a geometric factor. The amplitude decay factor is roughly in reverse proportion to the distance traveled. Waves suffer from friction or heat loss absorption while passing through a homogeneous medium. Transmission loss and energy loss caused by scattering are negligible in the case of a single reflection boundary with a smooth surface in a homogeneous medium. Many methods have been proposed for estimating absorption characteristics in the laboratory[11][12][13]. Here, the spectrum ratio method[14] is used.

4. 2. 1. **Spectrum ratio method**

The amplitude spectrum obtained by the Fourier transform of a wave traveling from a source to distance d is defined as $A(f)$. $A(f)$ is expressed from $A_0(f)$ of an amplitude spectrum of reference wave.

$$A(f)=A_0(f)\cdot G\cdot \exp\{-\gamma(f)\cdot d\} \tag{1}$$

Where f: frequency, $\gamma(f)$: frequency-dependent attenuation function, d : distance, G: geometric factor.

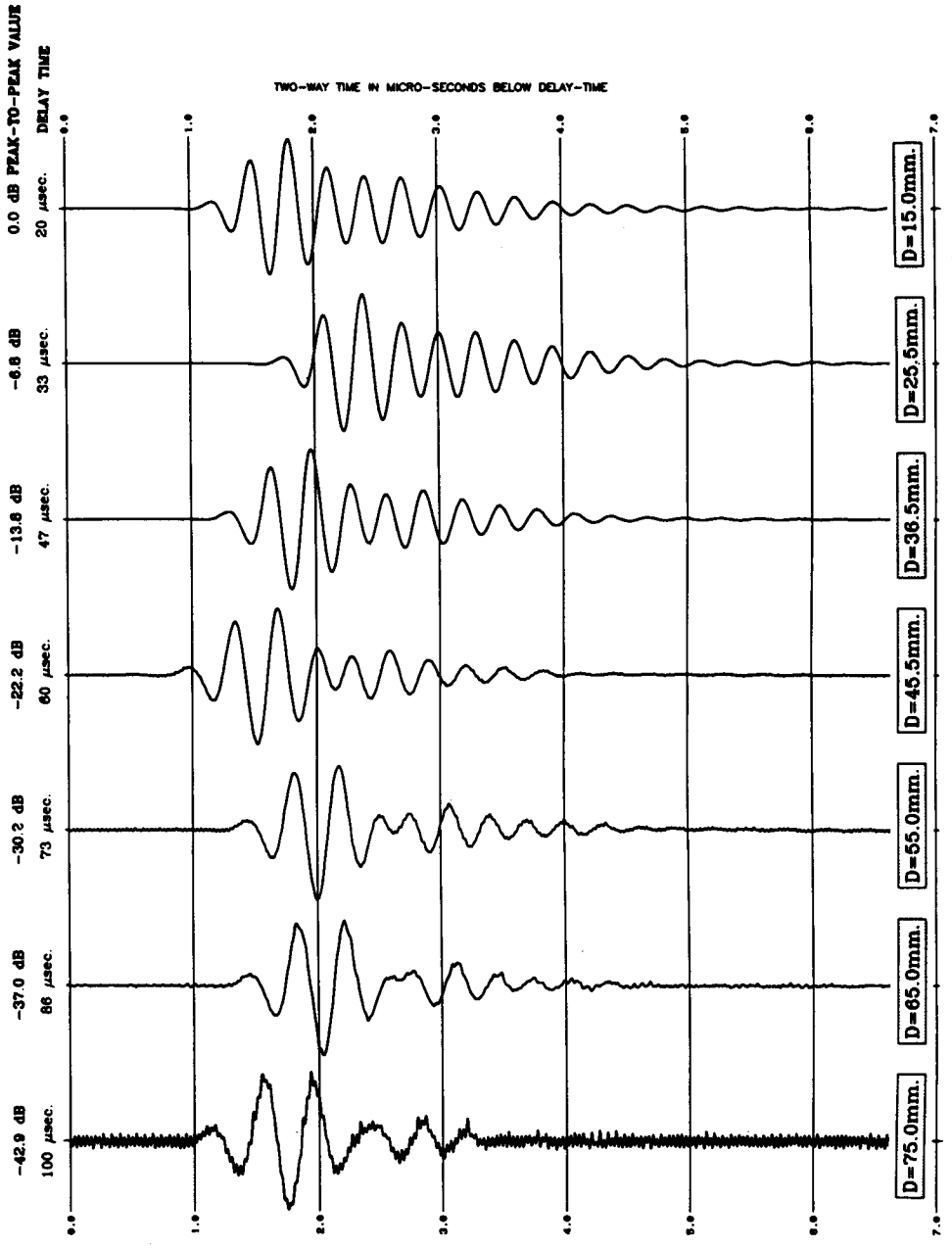

Fig. 13 Observed reflected waves from acrylic plate submerged in castor oil at various depths

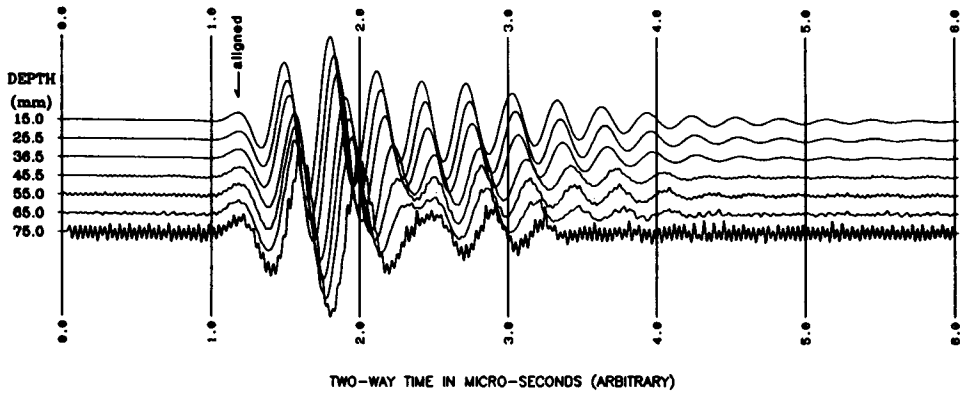

Fig. 14 Reflected waves which first arrivals in each trace in Fig. 13 are aligned

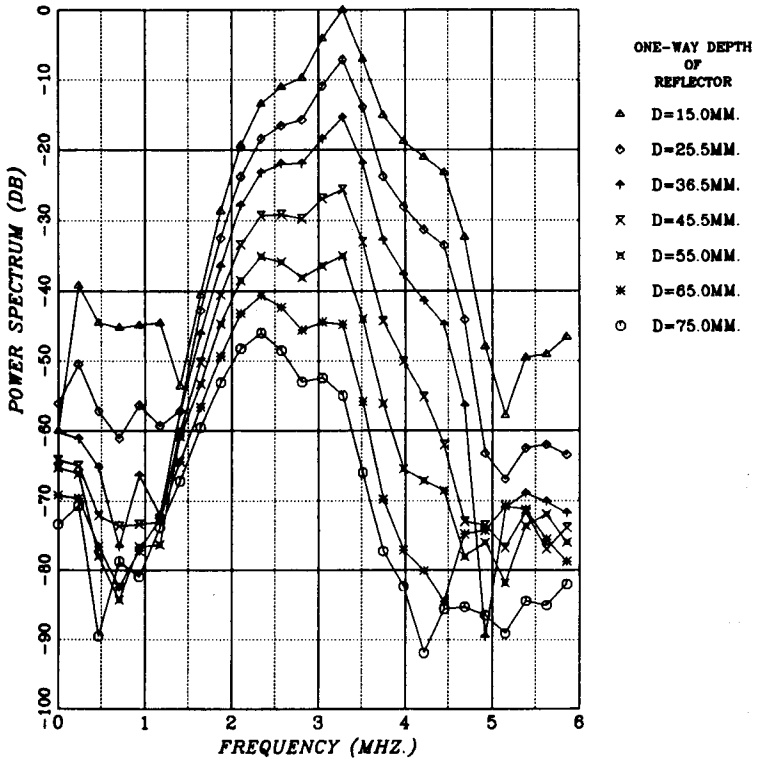

Fig. 15 Power spectra derived from reflected waves in Fig. 13

Attenuation function $\gamma(f)$ is assumed to be proportional to frequency[15)16)17)].

$$\gamma(f)=\alpha \cdot f, \tag{2}$$

Where, α is an estimated attenuation coefficient.
The substitution of (2) into (1) yields

$$A(f)=A_0(f) \cdot G \cdot \exp(-\alpha\, fd) \tag{3}$$

Define $R(f)$ as the ratio of amplitude spectra of waves at distances d_1 and d_2.

$$R(f)=A_2(f) / A_1(f) \tag{4}$$

The insertion of (3) into (4) yields

$$R(f)=\exp\{-\alpha f(d_2-d_1)\} \cdot G_2/G_1 \tag{5}$$

Take a natural logarithm of both sides of (5).

$$\ln R(f)=-\alpha(d_2-d_1)f+\ln\ (G_2/G_1) \tag{6}$$

If $d_2>d_1$, $R(f)<1$ and $G_2/G_1<1$. Thus, by setting $B(f)$ and b_0 by Equation (7),

$$\begin{aligned} B(f)&=-\ln R(f) \\ b_0&=-\ln(G_2/G_1) \end{aligned} \tag{7}$$

Equation (6) is expressed as

$$B(f)=\alpha(d_2-d_1)f+b_0 \tag{8}$$

The unit for $B(f)$ is neper and the unit for attenuation coefficient is nepers/MHz /cm. The attenuation can be expressed by another unit dB. By taking a common logarithm of both sides of Equation (5) and multiplying by 20, Equation (9) is derived.

$$20\log R(f)=-20\alpha(d_2-d_1)f \cdot \log e+20\log\ (G_2/G_1) \tag{9}$$

By setting $B'(f)$, b'_0 and α' by Equation (10),

$$\begin{aligned} B'(f)&=-20\log R(f) \\ b'_0&=-20\log\ (G_2/G_1) \\ \alpha'&=20\alpha\log e=8.686\alpha \end{aligned} \tag{10}$$

Equation (9) is written in Equation (11).

$$B'(f)=\alpha'\,(d_2-d_1)f+b'_0 \tag{11}$$

The units used for $B'(f)$ and α' are dB and dB/MHz/cm. Equations (8) and (11) show that the linear relationship is established between $B(f)$ or $B'(f)$ and frequency f, and that the attenuation coefficient α is calculated from a linear line slope determined by the least square method. There is another non-dimensional factor called quality factor for representing the attenuation. Quality factor is defined as

$$Q=2\pi W/\Delta W, \tag{12}$$

where Q: quality factor, W: maximum strain energy stored during one period of wave, ΔW: energy loss during one period. Here, regard the propagating plane wave u which is expressed as

$$u=A_0 \exp(-\gamma x) \cdot \cos 2\pi f(t-x/V), \tag{13}$$

where, x: distance, V: velocity, f: frequency, γ: attenuation function in Equation (2). By defining the energy as the square of amplitude, W and ΔW in Equation (12) are given by

$$\begin{aligned} W&=\{A_0 \exp(-\gamma x)\}^2_{(x=0)}=A_0^2 \\ \Delta W&=A_0^2-\{A_0 \exp(-\gamma x)\}^2_{(x=\lambda)} \\ &=A_0^2\{1-\exp(-2\gamma\lambda)\}, \end{aligned} \tag{14}$$

where, λ: wavelength

The substitution of Equation (14) into Equation (12) yields

$$\begin{aligned} Q&=2\pi W/\Delta W=2\pi A_0^2/A_0^2\{1-\exp(-2\gamma\lambda)\} \\ &\fallingdotseq 2\pi/\{1-(1-2\gamma\lambda)\}=2\pi/2\gamma\lambda \\ &=\pi/\gamma\lambda \end{aligned} \tag{15}$$

The insertion $V=f\lambda$ into Equation (15) yields

$$Q=\pi/\gamma\lambda=\pi f/\gamma V=\pi/\alpha V \tag{16}$$

By setting the depth d_1, d_2 and the travel time t_1, t_2 for calculating the spectrum ratio, Equation (16) is rewritten as

$$Q=\pi/\alpha V=\pi(t_2-t_1)/\alpha(d_2-d_1) \tag{17}$$

and since t_1 and t_2 are the two way travel times, d_1 and d_2 should be multiplied by 2. Equation (17) shows that if the attenuation function γ is proportional to frequency f, quality factor is independent of frequency.

4. 2. 2. **Estimating the attenuation coefficient of castor oil**

Figure 16 is a plot of attenuation in dB versus frequency at each depth. The attenuation is derived from the ratio of the amplitude spectra of the reflected waves at each depth to that of the reflection at the reference depth of 15.0 mm. Figure 16 also shows that the linear relationship is established between attenuation and frequency in the range from 1.5 to 4.5 MHz for each depth, and that the linear line slope increases with depth. This means that the amount of attenuation increases with depth. Figure 17 shows that the attenuation rate divided the attenuation in Figure 16 by the equivalent two way depth, in dB/cm versus frequency. Figure 17 demonstrates that attenuation rate versus depth is generally proportional to frequency at each depth, which means that Equation (2) is reasonable. Since the frequency out of 1.5 to 4.5 MHz range is considered as noise on the basis of the frequency characteristics of the probe, the relationship between the attenuation and the frequency is established within this range.

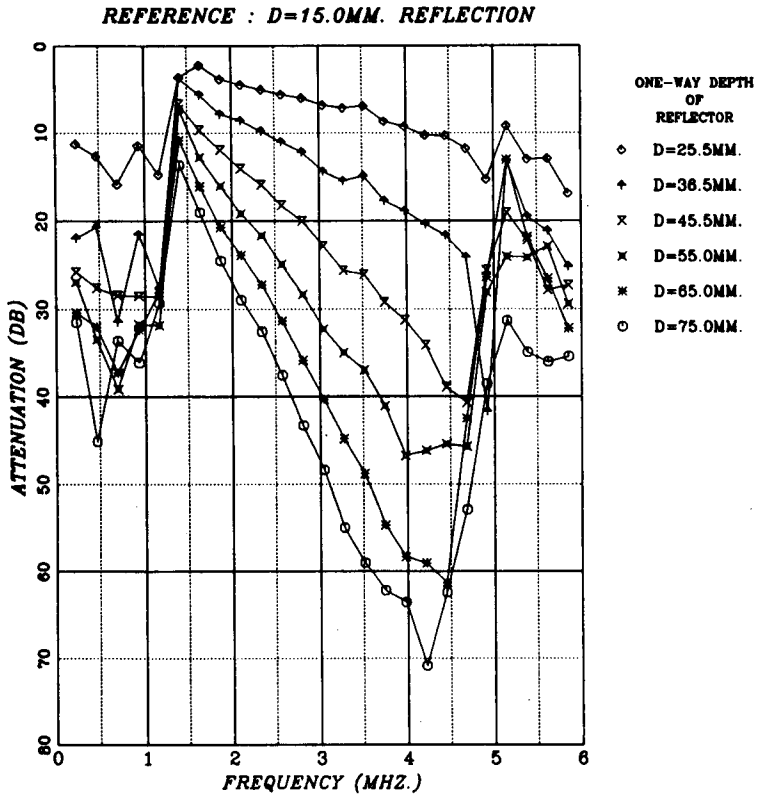

Fig. 16 Attenuation in dB versus frequency at each depth

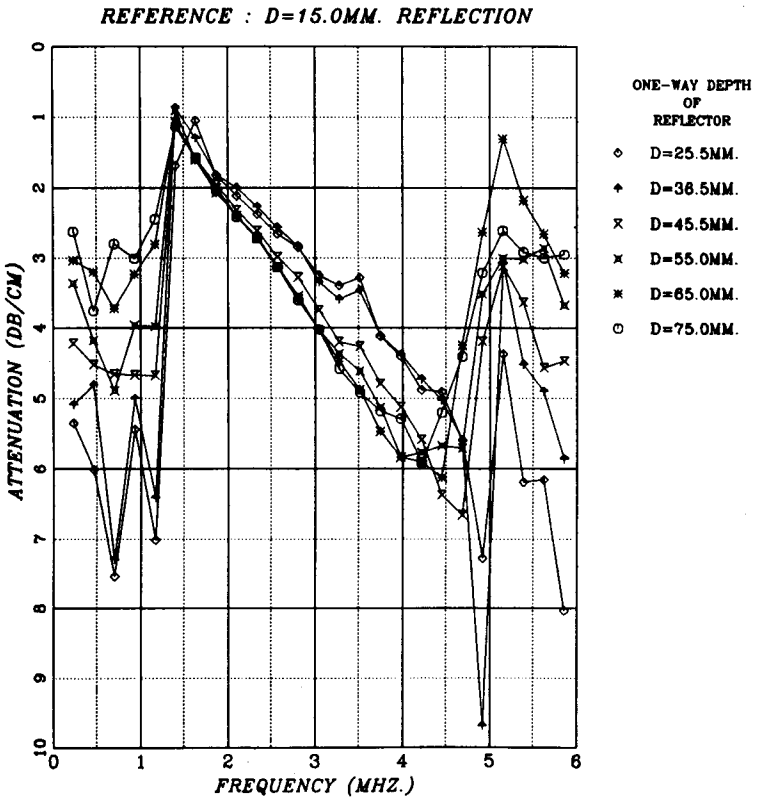

Fig. 17 Attenuation rate divided attenuation in Fig. 16 by equivalent two way depth, in dB/cm versus frequency

Table 6 Attenuation coefficients α, α' and Q factor derived from parameters in Fig. 18

$d/2$ (*mm*)	t (μsec)	d_2-d_1 (*cm*)	t_2-t_1 (μsec)	$\alpha'(d_2-d_1)$ (dB/MHz)	α' (dB/MHz/*cm*)	α (nepers/MHz/*cm*)	Q
15.0=d/2	21.067=t_1	0	0	—	—	—	—
25.5	34.634	2.1	13.567	2.625	1.250	0.144	141
36.5	48.184	4.3	27.117	5.745	1.336	0.154	129
45.5	60.834	6.1	39.767	9.970	1.634	0.188	109
55.0	74.300	8.0	53.233	13.843	1.730	0.199	105
65.0	87.300	10.0	66.233	17.713	1.771	0.204	102
75.0	101.000	12.0	79.933	20.230	1.686	0.194	108
				MEAN	1.568	0.181	116

Figure 18 shows the linear relations determined by the least square method between the attenuation function and the frequency. The attenuation coefficients α, α' and quality factor Q shown in Table 6 are calculated from the slope of these lines using Equations (11), (10) and (17). Figure 19 is a plot of $\alpha'(d_2-d_1)$ versus the depth difference d_2-d_1 in Table 6. By adding the attenuation rate value 0 at the depth difference 0, the attenuation coefficient α' is determined as 1.78 dB/MHz/cm from the least square method. This value corresponds to $\alpha=0.205$ nepers/MHz/cm and $Q=103$ in the case where the velocity in castor oil is assumed to be 1,490 m/s.

4. 3. **Basic wavelet extraction including absorption characteristics**

Waveforms at an arbitrary depth can be synthesized by using the estimated attenuation coefficient and the reflected waves at the reference depth of 15.0 mm.

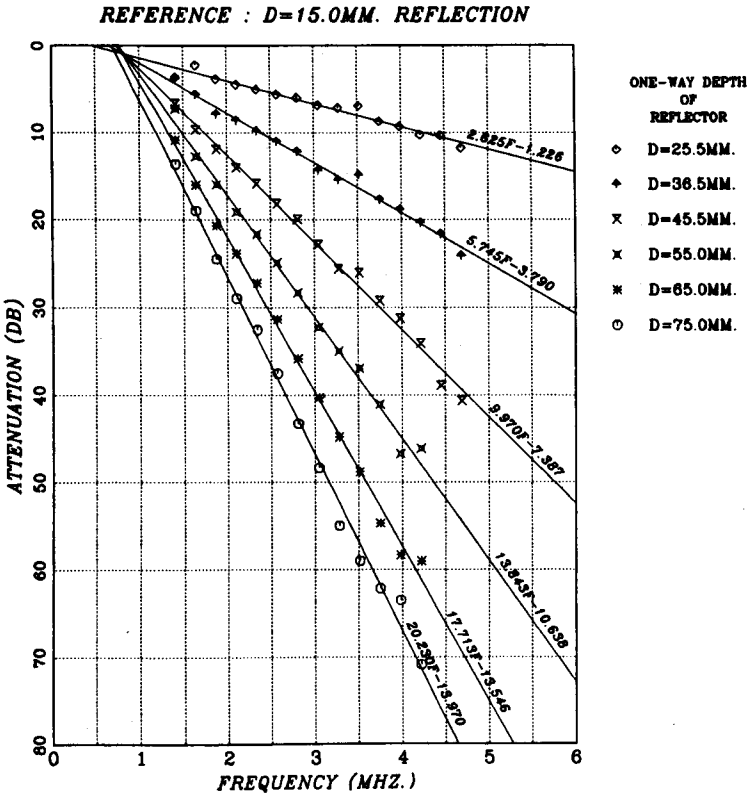

Fig. 18 Linear relationships between attenuation functions and frequency determined by least square method

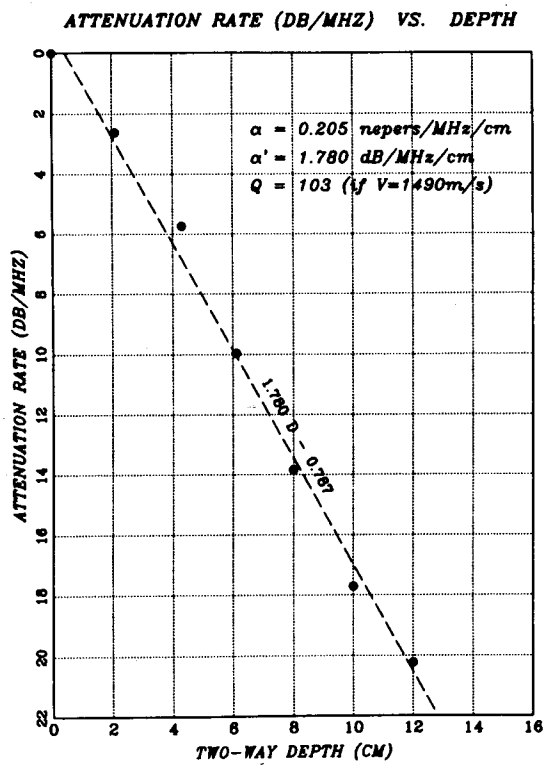

Fig. 19 Plot of $\alpha'(d_2-d_1)$ versus depth difference d_2-d_1 in Table 6

If the attenuation coefficient α' and the amplitude spectrum $A_1(f)$ at the two way depth, d_1, are known, the amplitude spectrum $A_2(f)$ at an other depth, d_2, is given from Equations (4), (10) and (11) as

$$A_2(f)=A_1(f)\cdot K\cdot 10^{-\alpha(d2-d1)f/20}, \tag{18}$$

where, $K=G_2/G_1$ of a geometric factor is an independent constant of frequency assumed to be 1. In order to remove the noise out of the 1.4 to 4.5 MHz range, the filter function $F(f)$ is applied to Equation (18).

$$A_2(f)=A_1(f)\cdot F(f)\cdot 10^{-\alpha'(d2-d1)f/20} \tag{19}$$

The applied filter function $F(f)$ is shown in Figure 20. If the amplitude spectrum and the phase spectrum are given, the reflected wave in a time domain can be synthesized by the Fourier transform. Here, assume that the phase spectrum at each depth is the same[18] as the one at the reference depth of 15.0 mm. This assumption means that the absorption characteristics do not affect the phase

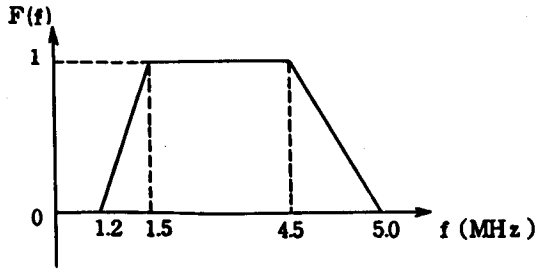

Fig. 20 Filter function in frequency domain

spectrum, though they do affect the amplitude spectrum. Figure 21 shows both the synthesized waveforms and the observed waveforms at each depth. Each trace is normalized with its maximum amplitude. The bold lines represent the synthesized waveforms, and the thin lines represent the observed waveforms. The waves in Figure 21 show good agreement, which means that both the method of estimating the attenuation coefficient and the assumption that the absorption characteristics do not affect the phase spectrum, are reasonable.

4. 4. Wavelet processing including the absorption characteristics

The basic wavelet takes a different waveform in the case of a medium of high absorption characteristics. Consequently, the basic wavelet, including the absorption characteristics, must be extracted for each depth in a wavelet processing. Figure 22 shows the result when the wavelet processing is applied to the reflection data from the acrylic plate in castor oil. Attenuation characteristics were not considered in this case. Figure 22(a) represents the originally observed waves for each depth. Figure 22(b) shows the result when a wavelet processing by the minimum phase conversion and a whitening deconvolution filter are applied. Figure 22(c) shows the result when a band pass filter with a pass band of 1.0 to 5.0 MHz is applied to Figure 22(b). Here, the reflected wave at depth of 15.0 mm was used as the basic wavelet in the wavelet processing. The record section in Figure 22(b) shows that the waveforms gradually change with depth from an impulse of desired wavelet to the waveforms with many sidelobes. This means that the reflected wave at depth of 15.0 mm is no longer suitable for the basic wavelet for deeper depths because of frequency dependent attenuation. Accordingly, synthesized waves, which included the attenuation characteristics for each depth, were adopted as a new basic wavelet and a wavelet processing was applied. Figure 23 shows the results. Figure 23(a) is the same as the originally observed waves. Figure 23(b) represents the result when a wavelet processing by the minimum phase conversion and a whitening deconvolution

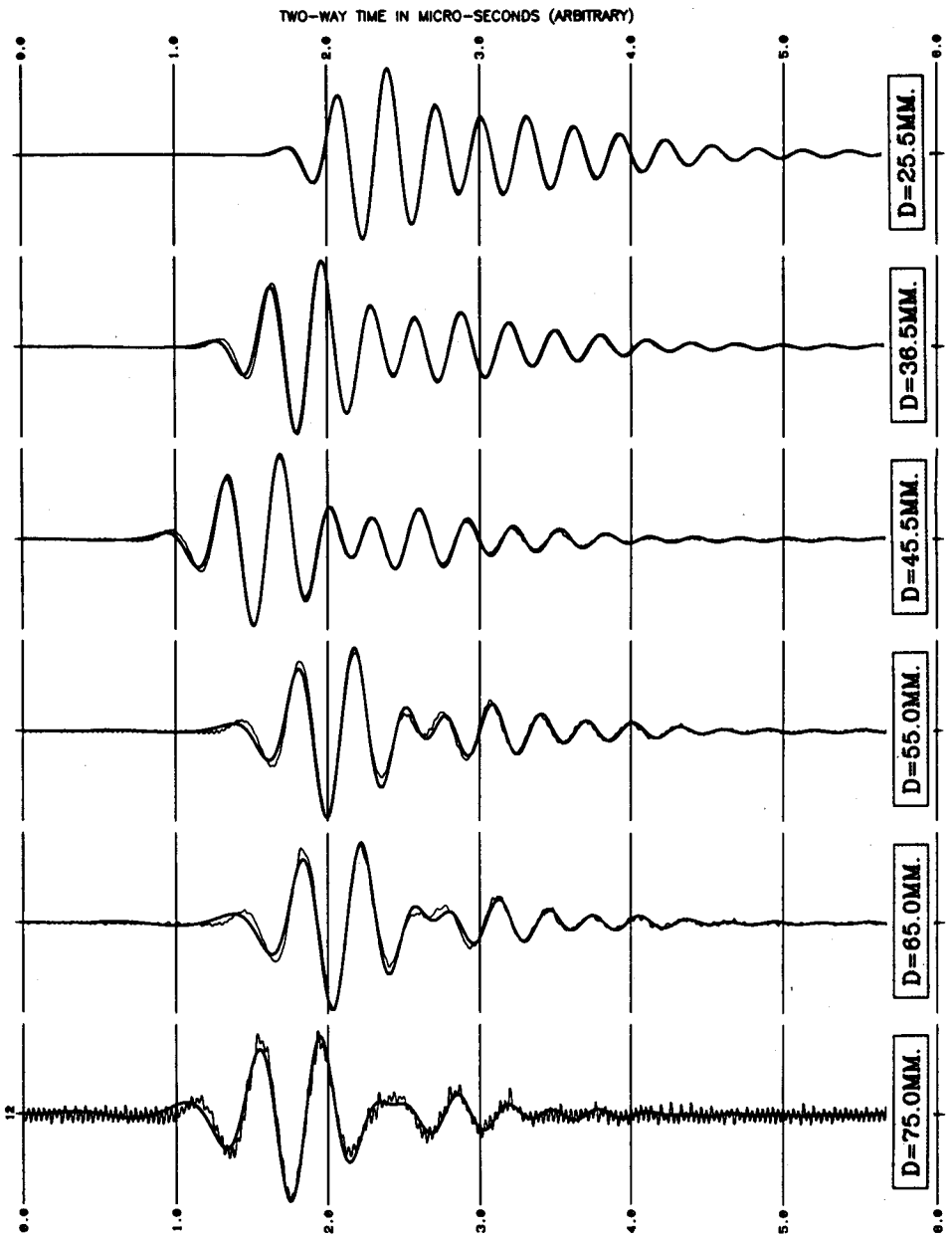

Fig. 21 Comparison between synthesized waves (bold lines) and actually observed reflected waves (thin lines)

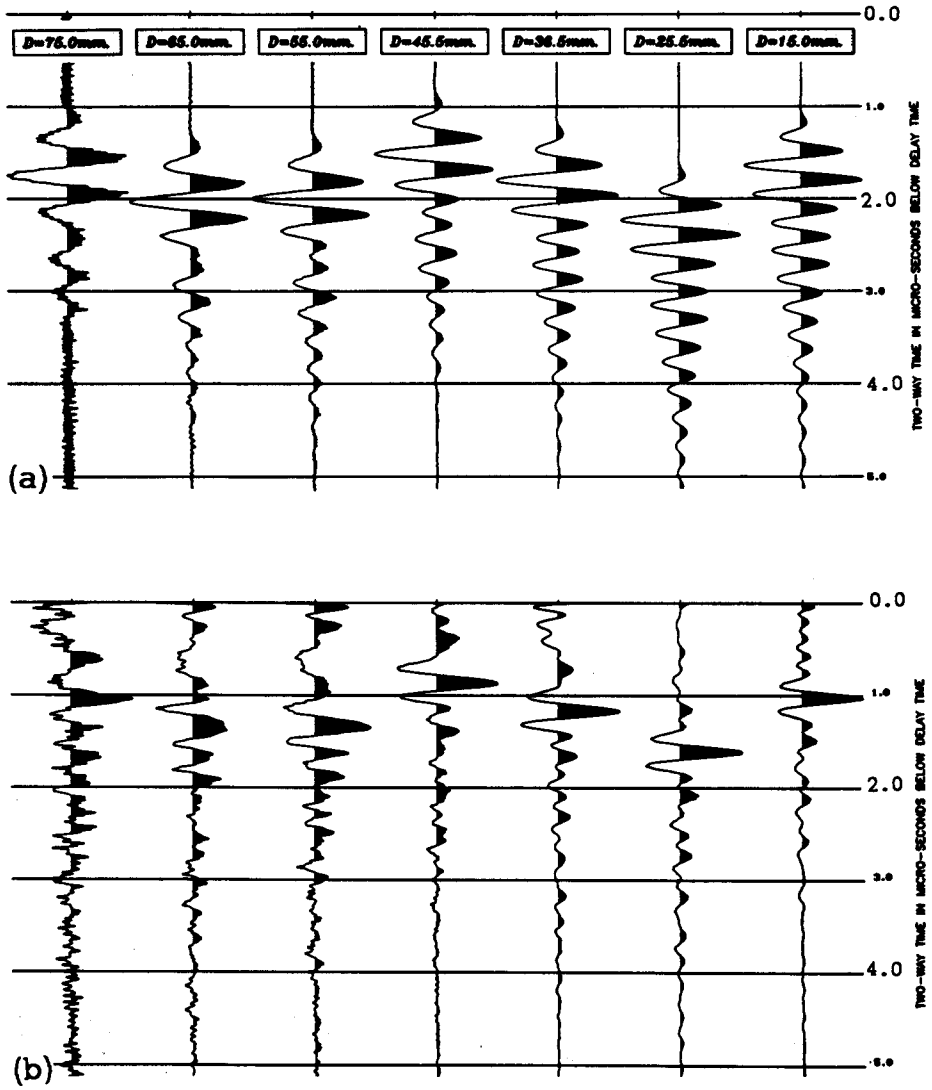
D=75.0mm.
D=65.0mm.
D=55.0mm.
D=45.5mm.
D=35.5mm.
D=25.5mm.
D=15.0mm.
0.0
1.0
2.0
3.0
4.0
5.0
TWO-WAY TIME IN MICRO-SECONDS BELOW DELAY TIME
(a)
(b)

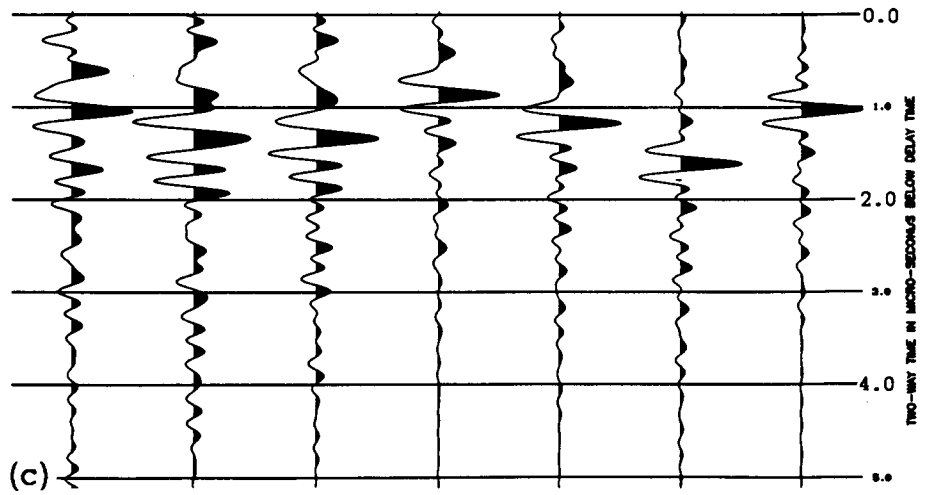

Fig. 22 Record sections when wavelet processing is applied to reflected waves at various depths without considering attenuation characteristics. Waveform at depth of 15.0 mm is used as basic wavelet

(a) original record

(b) record after applying wavelet processing and whitening deconvolution filter to (a)

(c) final record after applying band pass filter to (b)

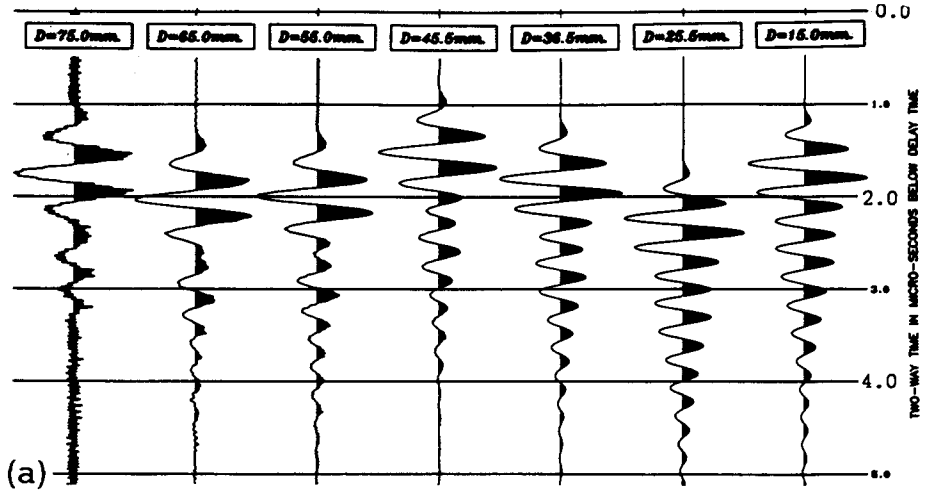

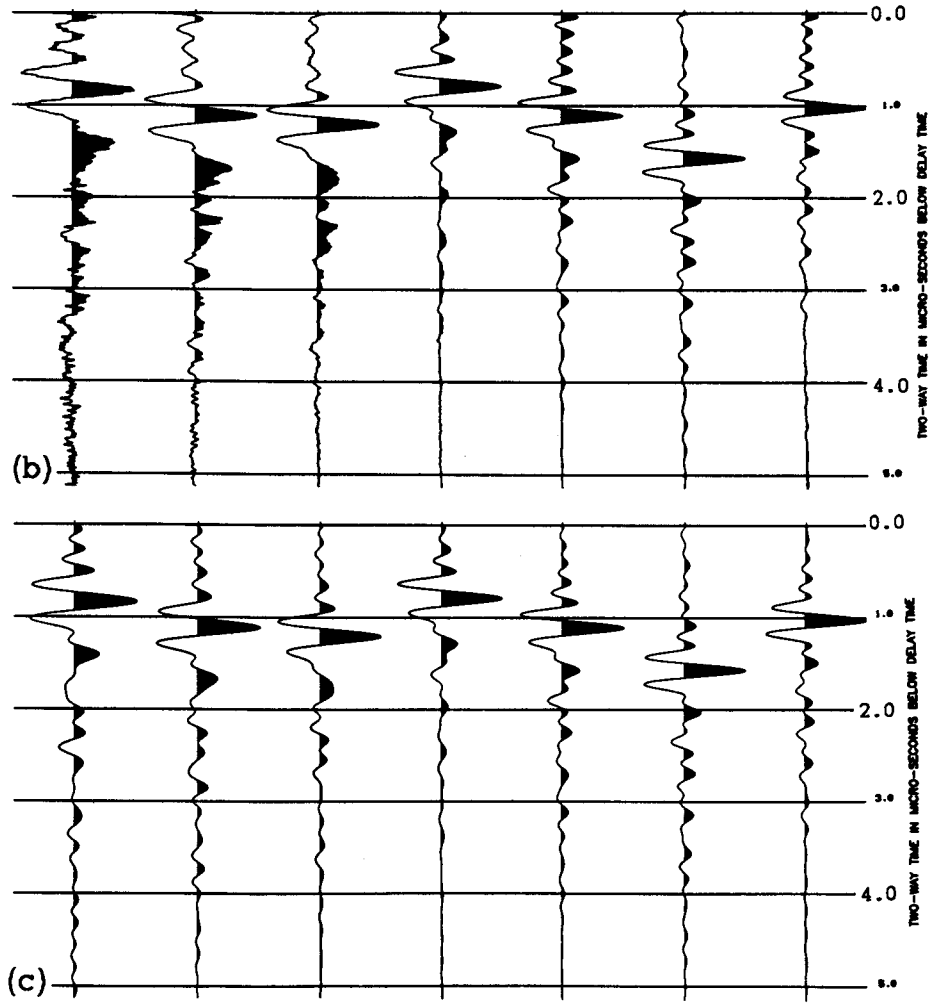

Fig. 23 Record sections when wavelet processing including absorption characteristics is applied. Synthesized waveforms in Fig. 21 are used as basic wavelet for each depth.

(a) original record

(b) record after applying wavelet processing and whitening deconvolution filter to (a)

(c) final record after applying band pass filter to (b)

filter were applied. Figure 23(c) shows the result when a band pass filter with a pass band of 1.0 to 5.0 MHz was applied to Figure 23(b). Figure 23(c) shows remarkable improvement, especially at deeper depths, when compared to Figure 22(c).

5. Experiment Using a Phantom Model

5. 1. Data acquisition

Data acquisition was performed using the multi-purpose tissue/cyst phantom shown in Figure 24. This phantom has the same attenuation, scattering characteristics and propagating velocity as liver parenchyma. Also, several size simulated cysts, encased cyst-like objects and solid tumor-like objects are included.

First, the data for estimating the attenuation characteristics of a phantom were acquired using Target C in the phantom model. Target C indicated by C in Figure 24 is a series of monofilament nylon rods 0.375 mm in diameter, starting at a distance 8 mm from the surface, 1 cm apart in a vertical plane. The reflected waves from the nylon rods at a distance 8.0 to 9.8 mm were observed by the probe placed just over Target C.

Second, the data for checking whether blood vessels in diameter 10 mm can be resolved or not, are observed using Target H. In Target H, a cyst-like object is encased in a highly reflecting plastic skin with a thickness of 0.02 mm. The twenty shot records were observed with the 400% CDP coverage by the eight

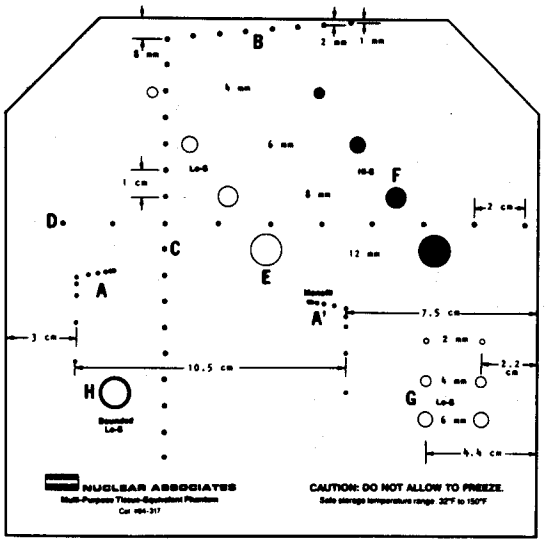

Fig. 24 Multi-purpose tissue/cyst phantom

elements of the probe placed just over Target H. The schematic diagram and the survey parameters for Target H are shown in Figure 25 and in Table 7.

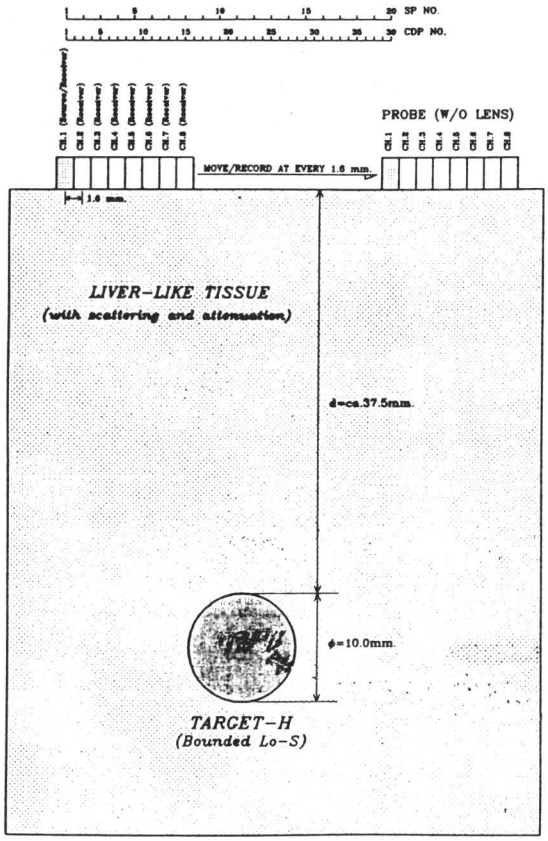

Fig. 25 Fluid-filled objects 10 mm in diameter and schematic diagram of data acquisition geometry

Table 7 Survey parameters for CDP stack

No. of channels	8
Channel intervals	1.6mm
CDP multiplicity	400%
Acoustic lens	No
Electronic focus	No
Amplifier gain	20dB

5. 2. **Estimating attenuation characteristics of a phantom**

The attenuation characteristics were estimated using the spectrum ratio method described in paragraph 4. 2. 1 . . Figure 26 shows the attenuation in dB for each depth normalized with the data at a depth of 8.0 mm, and the linear approximation by the least square method within 1.5 to 4.7 MHz. Figure 27 shows the attenuation coefficients in dB/MHz/cm for each depth, calculated from the linear line slopes in Figure 26 and their linear approximations. The determined attenuation coefficient for a phantom is 0.596 dB/MHz/cm.

5. 3. **Applying various data processings**

The data from Target H were submitted to data processing by a wavelet processing, a CDP stack, a migration processing and a synthetic acoustic impedance log.

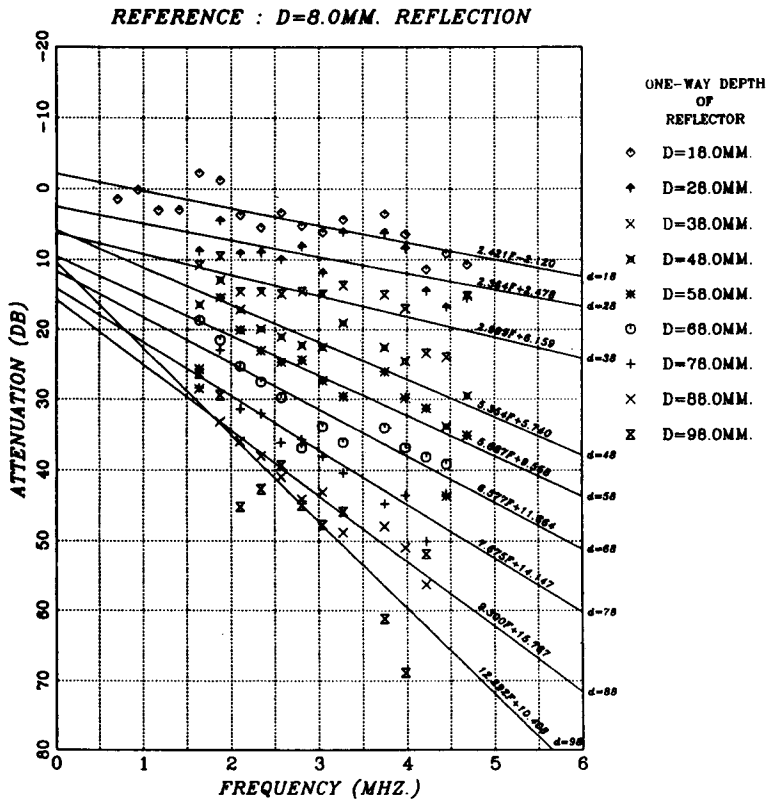

Fig. 26 Attenuation in dB for each depth, normalized with data at depth of 8.0 mm and linear approximation by least square method within 1.5 to 4.7 MHz

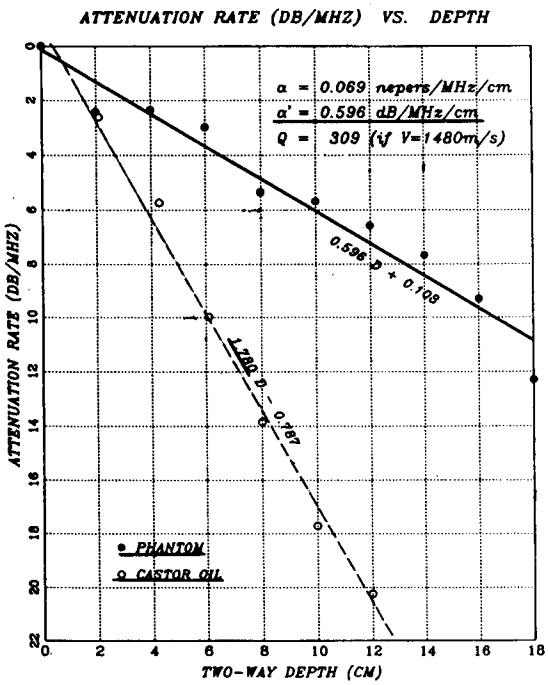

Fig. 27 Attenuation coefficient in dB/MHz/cm for each depth and its linear approximation

5. 3. 1. **Wavelet processing and CDP stack**

Figure 28 shows the near trace record selected from the CDP ensemble. Figure 29 shows the result when a wavelet processing, a 400% CDP stack and a band pass filter were applied. The most suitable scale factors for plot were adopted in each trace. The basic wavelet in the wavelet processing at a depth of 37.5 mm for Target H was synthesized, using both the reflected wave from the acrylic plate and the attenuation coefficient 0.596 dB/MHz/cm for the present phantom. The velocity distributions for the normal moveout correction were determined by the constant velocity scan method shown in Figure 30. The resolution of the reflections in Figure 29 shows a remarkable improvement over Figure 28. However, the S/N ratio is not improved. The reason for this is that the observed record contains a little noise which is removable by a band pass filter, because its frequency component differs from that of the signal.

5. 3. 2. **Migration processing**

The reflection time section generally represents the apparent structure fea-

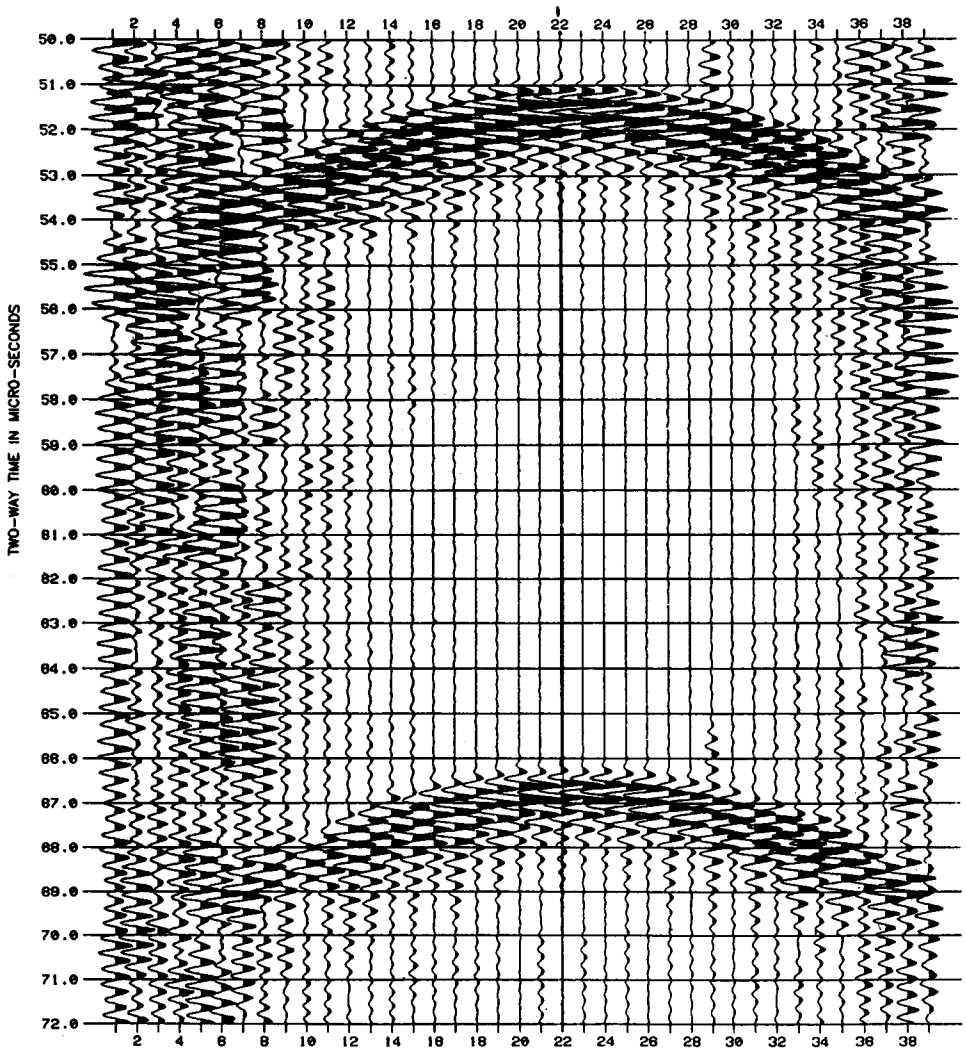

Fig. 28 Near trace section selected from CDP ensemble

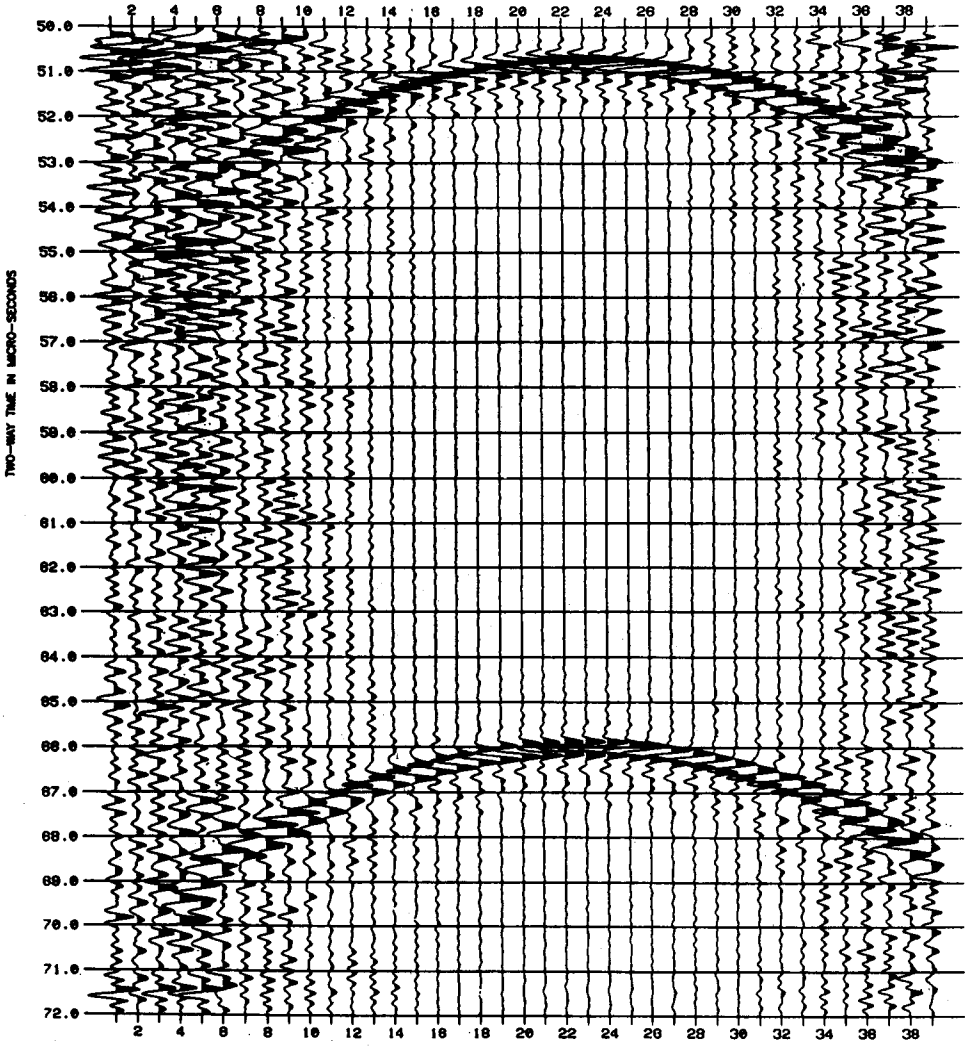

Fig. 29 Record section after applying wavelet processing, whitening deconvolution filter, 400% CDP stack and band pass filter

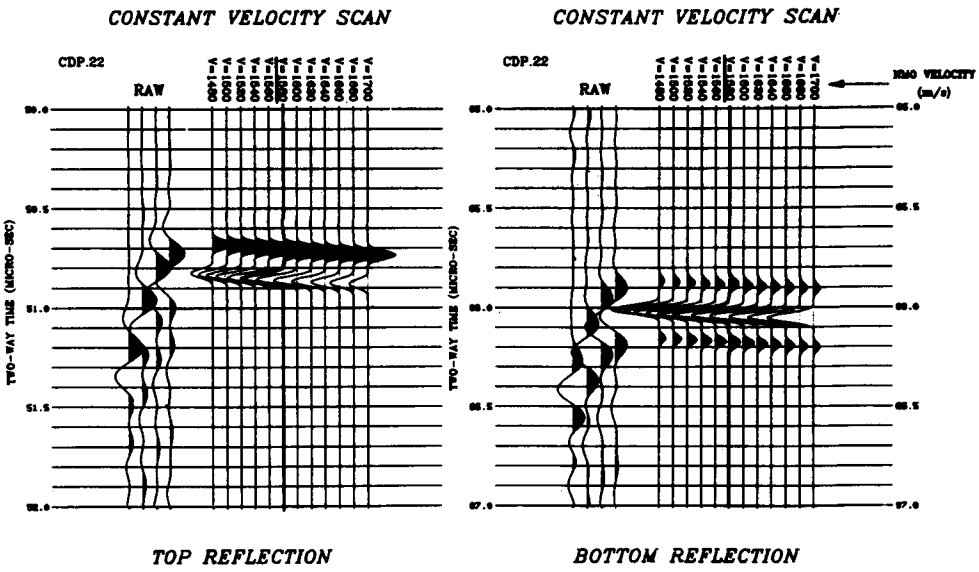

Fig. 30 Velocity analysis display using constant velocity scan method at CDP no. 22

ture in time domain for the actual structure. For example, the reflection time section for the structure in Figure 25 corresponds to the one in Figure 29. The operation for obtaining the true structure feature from the apparent one is called migration processing[19].

Here, the f-k migration method[20] was used. Figure 31 shows the record where one trace within each trace in Figure 29 is interpolated in order to avoid an aliasing effect during the f-k migration. Scaling was performed by the maximum value in whole traces to preserve the relative amplitude. Figure 32 shows the result when a migration processing was applied to the record in Figure 31, using the velocity determined from the velocity analysis. Figure 32 clarifies the true structure feature of Target H.

5. 3. 3. **Synthetic acoustic impedance log**

Figure 33 shows the synthetic acoustic impedance log[21] obtained by the integral of the amplitude of reflected waves. The vertical axis represents depth. Here, the velocity information derived from the velocity analysis was used for depth conversion. The depth of 40.5 mm for the top surface of Target H is deeper

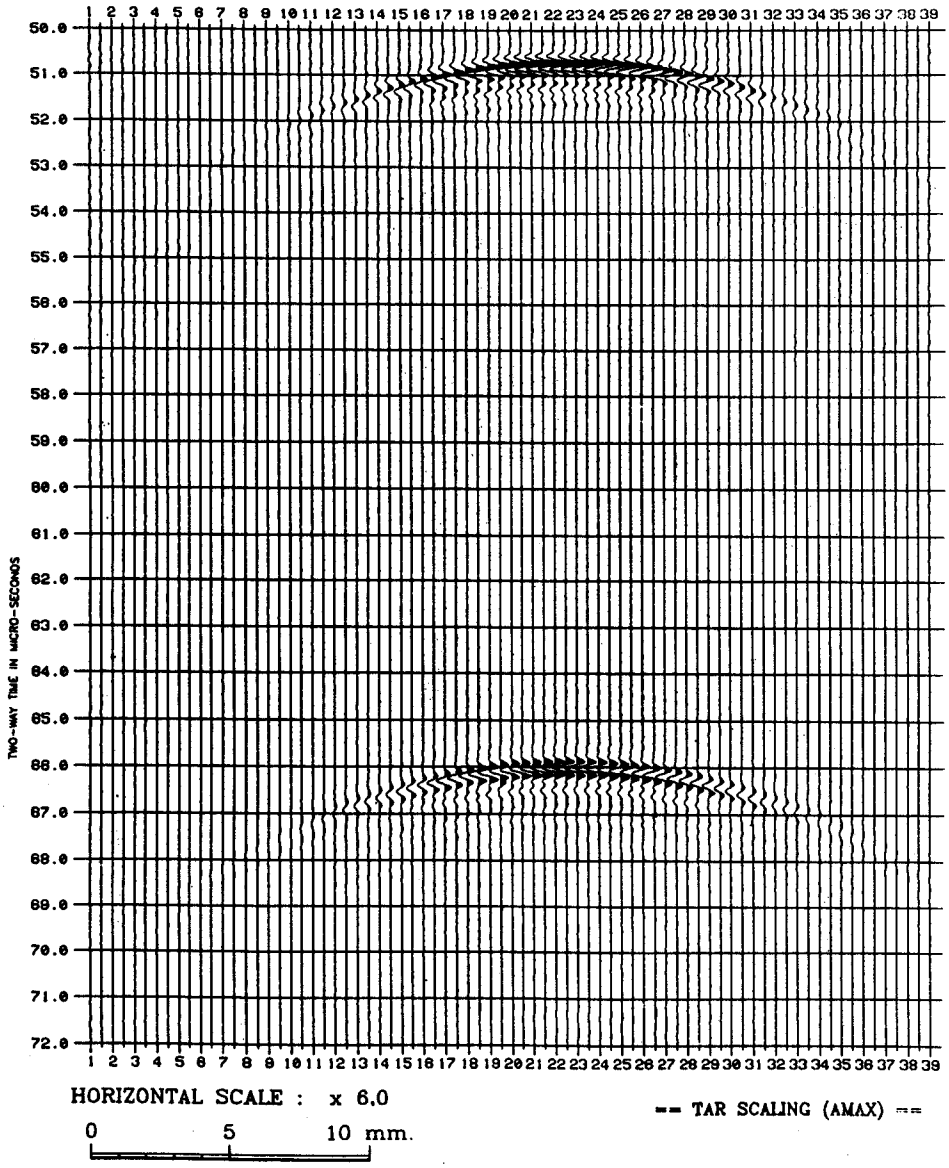

Fig. 31 Record section in which one trace within each trace in Fig. 29 is interpolated and is normalized by maximum value in whole traces

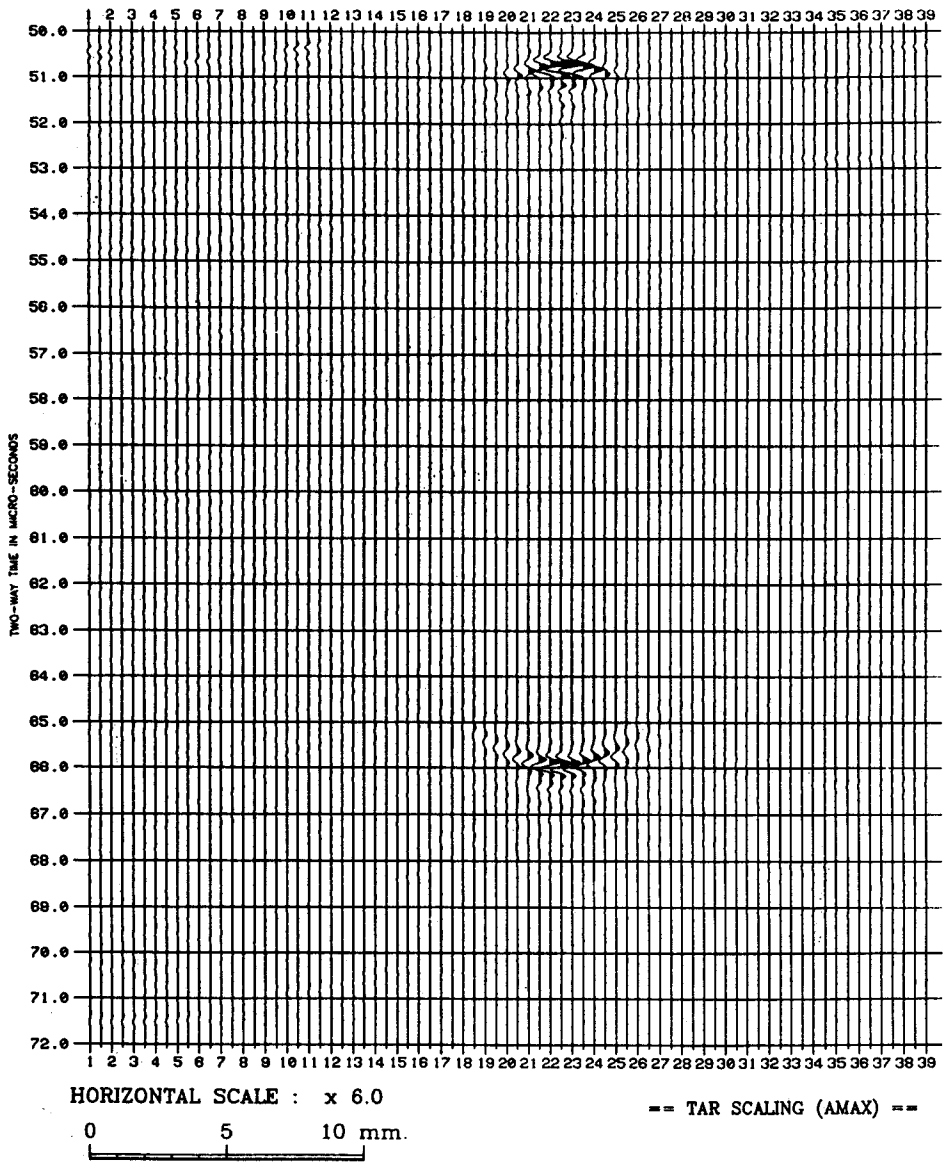

Fig. 32 Record section after applying f–k migration to data in Fig. 31

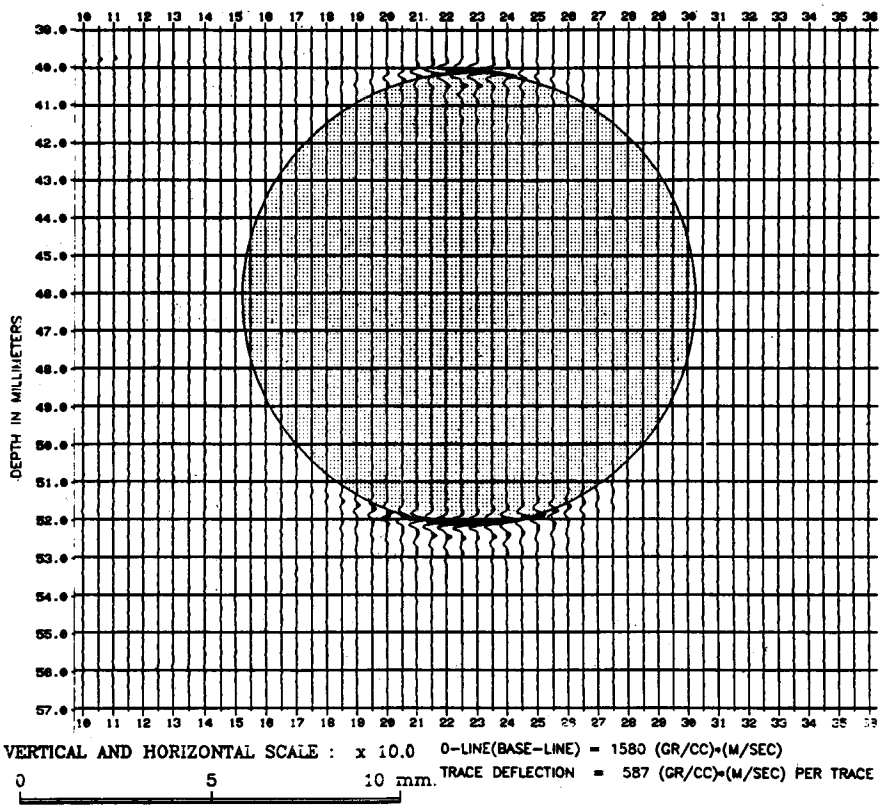

Fig. 33 Synthetic acoustic impedance log section generated from Fig. 32 by integration of reflection amplitude

by 2.5 mm than the actual depth of 37.5 mm. Also, the diameter of 12 mm is larger by 2 mm than the actual diameter which is 10 mm. These differences were caused by an error in the velocity used for depth conversion. If the point where the velocity analysis is performed shifts from just above Target H, the apparent velocity is higher than the actual velocity. The reason is that the velocity from the velocity analysis is multiplied by $1/\cos\theta$ in the case of a dipping reflection boundary with angle θ.

5. 4. **Polarity of reflected waves from Target H**

Target H is encased in a highly reflecting plastic skin with a thickness of

0.02 mm. The schematic reflection time series from both the top and the bottom of Target H is shown in Figure 34(a). Usually, the wavelet processing sequence includes a minimum phase wavelet conversion, a whitening deconvolution, a CDP stack and finally a band pass filter of zero phase. Consequently, the final record section is assumed to have zero phase characteristics. When the reflection time series in Figure 34(a) is given, the anticipated reflection record after the CDP stack is as Figure 34(c), which is the convolution of Figure 34(a) with (b). Here, Figure 34(b) shows the basic wavelet. Figure 34(d), (e) and (f) shows the

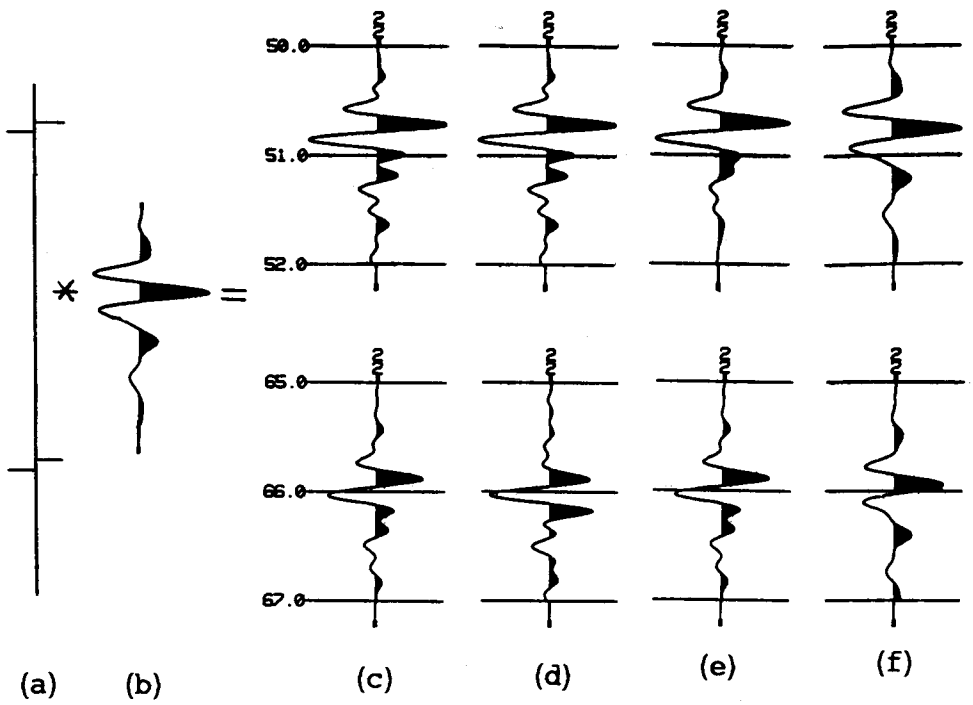

Fig. 34 Reflected waves from top and bottom of hole at each stage of data processing

(a) Schematic reflection time series from top and bottom of Target H

(b) zero phase waveform representing reflected wave after wavelet processing

(c) waveforms to be actually observed

(d) waveforms after applying wavelet processing to (c)

(e) waveforms after applying f-k migration to (d)

(f) synthetic acoustic impedance log

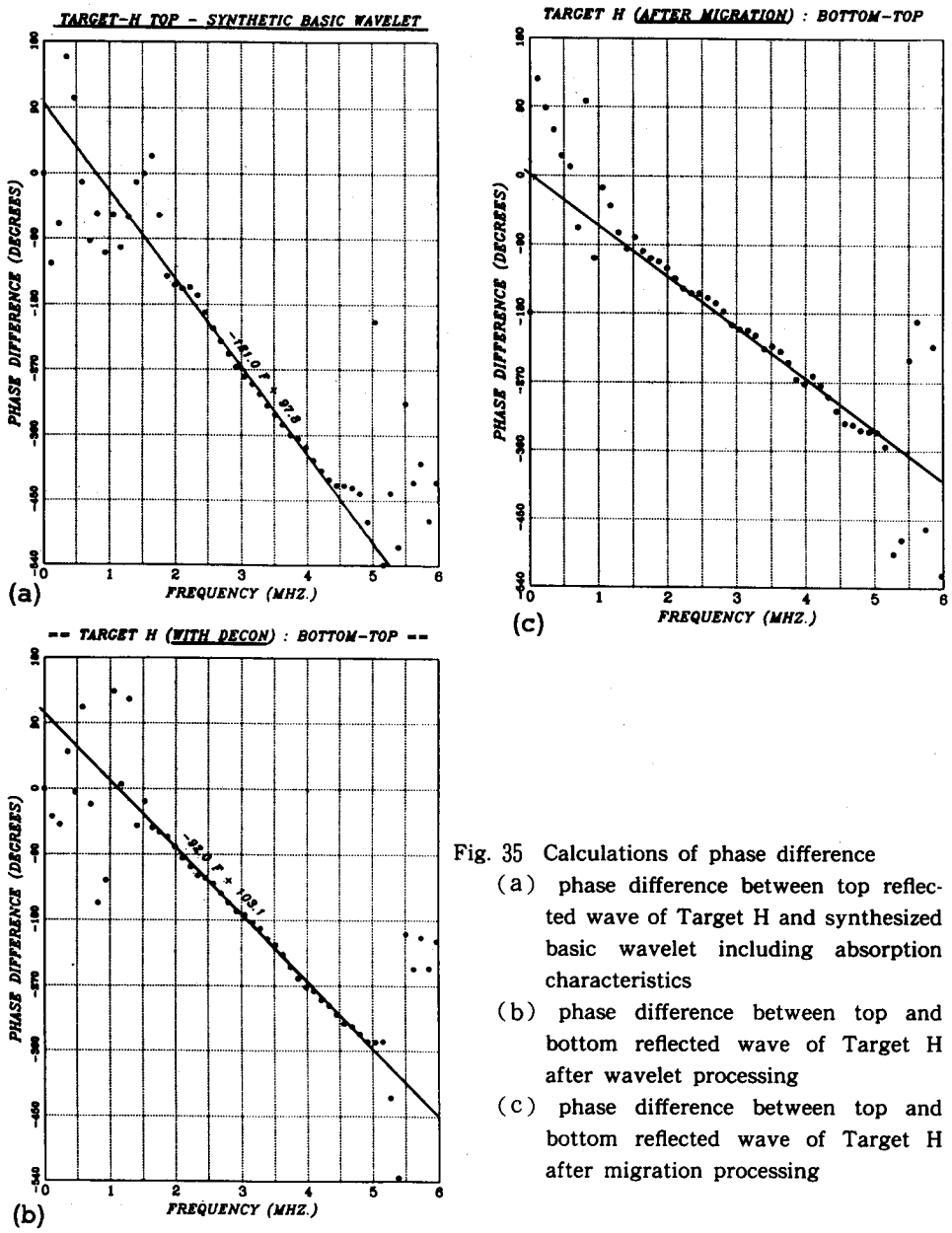

Fig. 35 Calculations of phase difference

(a) phase difference between top reflected wave of Target H and synthesized basic wavelet including absorption characteristics

(b) phase difference between top and bottom reflected wave of Target H after wavelet processing

(c) phase difference between top and bottom reflected wave of Target H after migration processing

actually observed record after a wavelet processing, a migration processing and a synthetic acoustic impedance log are applied in turn.

Here, consider the polarity of the reflected waves from both the top and the bottom of Target H, as shown in Figure 34(c) ~ (f).

(i) the reflected waves from the top of Target H in Figure 34(c) and (d) differ from those in Figure 34(b). The 0.02 mm thickness of the highly reflecting plastic skin of Target H corresponds to about 30 ns in time, which is almost twice the sample rate in the present experiment. The reflection time series in this case is represented in Figure 34(a). If a waveform passes through this time series, an output waveform becomes a differential wave of the input wave, and its phase is progressed by 90°. This relationship is also established for the reflection of the bottom in Figure 34(c) and (d). Figure 35(a) shows the phase differences versus the frequency of the top reflection in Figure 34(d) from the synthesized basic wavelet. The phase difference is given as 97.8° from the least aquare method by the data within 1.8 to 4.3 MHz.

(ii) Figure 35(b) shows the phase differences versus the frequency of the top reflection from the bottom one in Figure 34(d). The phase difference 103.1° determined by the least square method is close to 90° because the ray paths of the bottom reflection pass through a facus.

(iii) Figure 35(c) shows the phase difference versus the frequency of the top reflection from the bottom one in Figure 34(e). The phase difference is equal to 0° in this case. The reason for this is that a phase progress by 90° for passing through a focus is recovered by the migration processing.

(iv) The synthetic acoustic impedance logs for both the top and the bottom reflections in Figure 34(f) are very close to the symmetric zero phase waveform shown in Figure 34(b). This is because the phase is delayed 90° by an integral operation in the generation of the synthetic acoustic impedance logs.

6. Conclusions

Various processings were applied to data from an ultrasonic diagnostic instrument in order to improve the resolution. The following conclusions were obtained.

(i) Resolution was not only greatly improved, but polarity and phase information in the reflected waves were also preserved through wavelet processing and migration processing.

(ii) Velocity distribution in a medium was analysed by CDP stck data.

(iii) Wavelet processing, which utilizes synthesized wavelets at each depth as

the new basic wavelets including the absorption characteristics, gave a sharply improved resolution.

(iv) Fluid-filled objects 10 mm in diameter, such as the larger blood vessels or cysts, were resolved by wavelet processing and migration processing.

Acknowlegements

The author is indebted to Professor Dr. Koichi Sassa and Professor Dr. Soji Yoshikawa of Kyoto university for their encouragement and enlightening technical discussions.

The author also would like to thank Mr. Shiro Ohkawa and Mr. Ariaki Umedo of Japan Petroleum Exploration Co. Ltd. and Mr. Yoshikazu Terayama of Akashi Seisakusho Ltd. for their efforts in gathering data.

References

1) K. Nakayawa; Japanese Journal of Applied Physics, **43**, 721～727 (1980)
2) W. H. Mayne; Geophysics, **27**, 929～938 (1962)
3) E. A. Robinson; Geophysics, **32**, 418～484 (1967)
4) Y. Ashida; Butsuri-Tanko, **31**, 8～22 (1978)
5) M. H. Taner and F. Koehler; Geophysics, **34**, 859～881 (1969)
6) M. H. Taner, F. Koehler and R. E. Sheriff; Geophysics, **44**, 1041～1063 (1979)
7) P. Hubral; Geophysical prospecting, **24**, 478～491 (1976)
8) R. F. Stöckli; Geophysics, **49**, 767～770 (1984)
9) R. E. Sheriff and L. P. Geldart; "Exploration seismology", Cambridge University Press, New York, **1**, 112～117 (1982)
(10) D. H. Johnston and M. N. Toksöz; "Seismic wave attenuation", SEG, 105～114 (1981)
11) H. Spetzler and D. L. Anderson; J. Geophys. Res., **73**, 6051～6060 (1968)
12) L. Peselnick and I. Zietz; Geophysics, **24**, 285～296 (1959)
13) D. D. Jackson; Ph. D. Thesis, M. I. T. (1969)
14) M. N. Toksöz, C. H. Cheng and A. Timur; Geophysics, **41**, 621～645 (1976)
15) F. J. Mcdonal, F. A. Angona, R. L. Mills, R. L. Sengbush, R. G. Van Nostrand and J. E. White; Geophysics, **23**, 421～439 (1958)
16) L. Knopoff; Rev. Geophys. **2**, 625～660 (1964)
17) D. D. Jackson and D. L. Anderson; Rev. Geophys. Space Phys., **8**, 1～63 (1970)
18) R. E. White and P. N. S. O'Brien; Geophysical Prospecting, **22**, 627～651 (1974)
19) J. G. Hagedoorn; Geophysical Prospecting, **2**, 85～127 (1954)
20) R. H. Stolt; Geophysics, **43**, 23～48 (1978)
21) Y. Ishii; Butsuri-Tanko, **29**, 1～10 (1976)